redispersion steps were performed. Finally, the PEGylated nanoparticles were suspended in 10 mL of phosphate buffered solution (PBS) (pH = 7.4, I = 0.15 M) containing 0.05 wt % bovine serum albumin (BSA).

The dispersion stability of the PEGylated gold nanoparticles and their lectin-induced aggregation were evaluated spectrophotometrically by UV−visible spectrophotometer (V-550 UV/VIS spectrophotometer, JASCO, Japan) at 25 °C. The normalized integrated absorbance (NIA)[11] between 600 and 750 nm was used as an indicator of the aggregate formation. The NIA is defined as follows:

$$\mathrm{NIA}(t) = (A_t - A)/A$$

where A is the initial integrated absorbance between 600 and 750 nm, and A_t is the integrated absorbance between 600 and 750 nm t hours after the addition of RCA_{120}.

Scanning Electron Microscopic (SEM) Measurements. To estimate the thickness of the PEG layer on the surface of the PEGylated gold nanoparticles, SEM images were taken at different acceleration voltages (4.7 and 1.0 kV) with a LEO 1550 electron microscope (Carl Zeiss, Germany). SEM samples were prepared by mounting a drop of the solution on carbon-coated Cu grids and allowing them to dry in the air. Image analyses to obtain average particle size and the size distributions were performed on a Macintosh Power Mac G4 computer using the public domain NIH Image program.[12]

Results and Discussion

Preparation of PEGylated Gold Nanoparticles with Varying Lactose Functionality. As shown in Scheme 1, the PEG dimer (acetal-PEG-S-)$_2$ (M_n = 12 000, MWD = 1.08) was prepared by a dimerization of acetal-PEG-SH through disulfide bonding in DMSO/MeOH. Acetal groups at both ends of (acetal-PEG-S-)$_2$ were then transformed into aldehyde groups by a gentle acid treatment, followed by the reaction with *p*-aminophenyl β-D-lactopyranoside in the presence of $NaBH_3CN$ to undergo a reductive amination. The lactose conversion ratio of the obtained polymer, (lactose-PEG-S-)$_2$ (M_n = 12 200, MWD = 1.08), was determined to be 65% based on the peak intensity ratio of the phenyl protons of the conjugated *p*-aminophenyl β-D-lactopyranoside (6.5~6.9 ppm) moiety to the methylene protons of the PEG chain (3.3~3.8 ppm) in the ^{1}H NMR spectrum (Supporting Information, Figure S1).

Then, the mixtures of PEG dimers, (acetal-PEG-S-)$_2$ and (lactose-PEG-S-)$_2$, in varying molar ratios were reacted with commercially available gold nanoparticles (diameter: 20 nm) at room temperature in distilled water overnight. To remove excess polymer in the solution, repeated centrifugation (42 000 × g) and redispersion were carried twice. Finally, the PEGylated nanoparticles were suspended in PBS (pH = 7.4, I = 0.15 M) containing 0.05 wt % bovine serum albumin (BSA).

Dispersion Stability of PEGylated Gold Nanoparticles. Availability of the PEG dimer, (acetal- or lactose-PEG-S-)$_2$, as effective PEGylation reagents of gold nanoparticles was confirmed from the redispersibility of the nanoparticles after centrifugation as well as from a profile of UV−visible spectra. PEGylated gold nanoparticles spun down at 42 000 × g for 30 min at 20 °C can be readily resuspended in deionized water as well as in PBS (pH = 7.4, I = 0.15 M). On the other hand, most of the bare gold nanoparticles were unable to be resuspended after the same centrifugation process. Then, the colloidal stability of (acetal-PEG-S-)$_2$-coated gold nanoparticles (lac0) was evaluated under the physiological salt condition (pH = 7.4, I = 0.15 M) by monitoring the change in the metachronic absorbance in the UV−visible spectrum. An aqueous solution of dispersed gold nanoparticles is red due to the surface plasmon absorbance centered around 523 nm in the optical spectrum. On the other hand, particle aggregation leads to the formation of a new absorption band at longer wavelengths than 600 nm.[3] Dispersion of lac0 in PBS (pH = 7.4, I = 0.15 M) indeed maintained an absorption maximum unchanged around 523 nm without any emergence of new absorption bands at larger wavelengths characteristic of aggregates. Nevertheless, there is a gradual decrease in the relative absorbance at 523 nm with time due to a decrease in the particle concentration resulting from the adsorption of the nanoparticles on the glass wall of the vessel. To prevent lac0 from adsorbing on the vessel wall, a small amount of bovine serum albumin (BSA) was added into the solution. As shown in Figure 1, the addition of 500 μg/mL (0.05 wt %) BSA completely inhibited this nonspecific adsorption of the nanoparticles to the vessel wall, allowing a highly stable dispersion of PEGylated gold nanoparticles in physiological salt condition to be obtained. Note that bare gold nanoparticles in PBS with 0.05 wt % BSA rapidly underwent aggregation to have an appreciable increase in the absorbance of around 650 nm (data not shown).

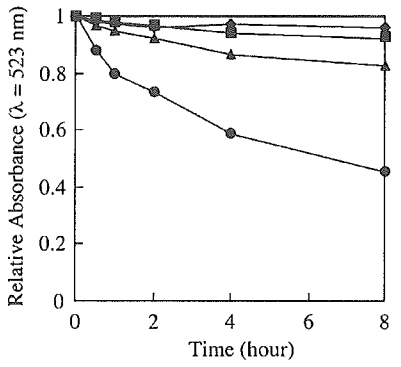

Figure 1. Dispersion stability of PEGylated gold nanoparticles in PBS (pH = 7.4, I = 0.15 M) containing several concentration of bovine serum albumin (BSA), (●) 0 μg/mL; (▲) 50 μg/mL; (■) 200 μg/mL; (♦) 500 μg/mL.

Characterization of PEGylated Gold Nanoparticles Possessing Regulated Density of Lactose on the Distal End of PEG Strands. The number of PEG chains immobilized on a single gold nanoparticle was determined by thermogravimetric analysis (TGA). A clear decrease in the weight of lac0 was observed in the TGA curve in the range of 300~400 °C due to the thermal decomposition of PEG moieties.[13] Then, the number of PEG chains on each gold nanoparticle was calculated to be 520, using the concentration of gold nanoparticles (7.0 × 10^{11} particles/mL) provided by the manufacturer and the weight-loss due to PEG decom-

Table 1. Number of PEG Chain and Ligand Density on Gold Nanoparticles Estimated from the Results of TGA and SEM

lactose functionality (%)	20	40	65
number of lactose molecules on 1 particle	104	208	338
area occupied by 1 lactose molecule (nm^2)[a]	34	17	10
average distance between lactose moieties (nm)[b]	5.8	4.1	3.2

[a] Surface area of PEGlyated gold nanoparticles ($4\pi(33.3/2)^2$ nm^2) was divided by number of lactose molecules on a single particle. [b] Square root of area occupied by 1 lactose molecule.

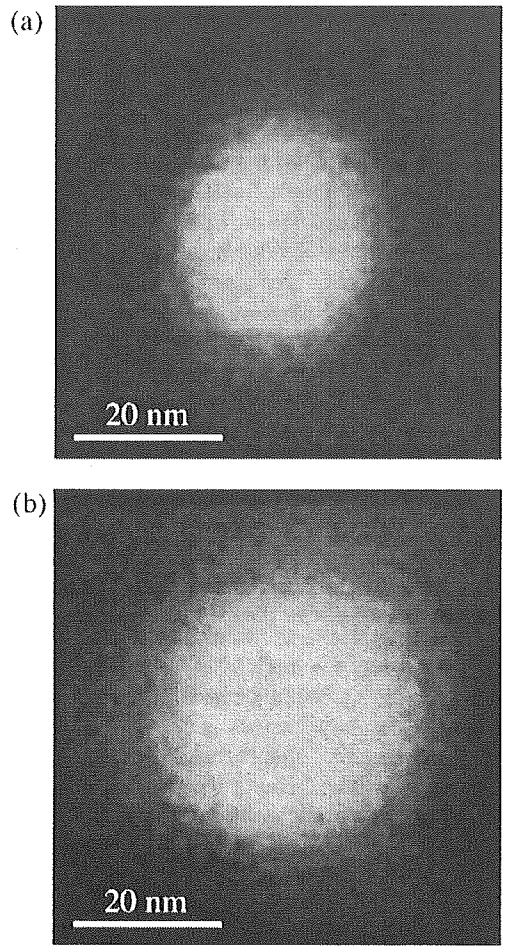

Figure 2. SEM images of PEGylated gold nanoparticles. The acceleration voltages are (a) 4.7 and (b) 1.0 kV, respectively.

position measured by TGA. Based on this calculation, the number of lactose molecules on a single gold nanoparticle was also determined as summarized in Table 1.

Scanning electron microscopy (SEM) was used to estimate the thickness of the PEG layer of PEGylated gold nanoparticles. Figure 2, parts a and b, shows SEM images photographed with 4.7 and 1.0 kV acceleration voltages, respectively. Note that secondary electrons were detected strongly from gold atoms at a higher acceleration voltage (4.7 kV), whereas at a lower acceleration voltage (1.0 kV), secondary electrons from the PEG layer were also detected. The average diameter of PEGylated gold nanoparticles was then determined to be 33.3 ± 2.8 nm (mean ± SD, $n = 914$) from the SEM images at 1.0 kV (Figure 2b) with NIH image software.[12] On the other hand, the diameter determined from the image taken at 4.7 kV was consistent with that of bare

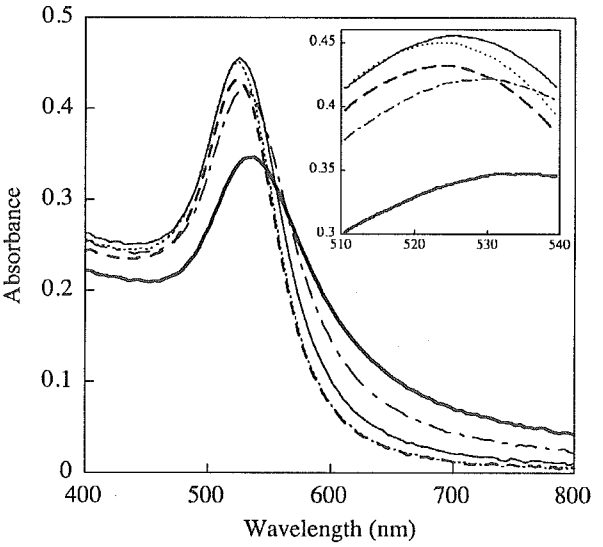

Figure 3. Change in the UV–vis spectra of lac65 with time after the addition of 200 μg/mL RCA_{120}. Dotted line 0 h; thin solid line 1 h; dotted-dashed line 2 h; thick solid line 4 h; and dashed line the spectrum after the addition of excess D-galactose (10 mg/mL) to 4 h. The insert is the expanded spectra between 510 and 540 nm.

gold nanoparticles (20 nm) provided by the manufacturer. Consequently, the thickness of the PEG layer on the gold nanoparticle was estimated to be ~7 nm. Note that the end-to-end distances (R) of PEG [$M = 6000$ g/mol, degree of polymerization (DP) = 136] based on zigzag, meander,[14] and random coil[15] models were calculated to be 47.6, 24.5–27.2, and 5.9 nm, respectively. Thus, it is likely that PEG strands immobilized on gold nanoparticles may adopt a conformation of slightly stretched random coil. Consequently, lactose densities and the average distances between lactose moieties on lac20, lac40, and lac65 were calculated from SEM and TGA data and are summarized in Table 1. These density and distance values, calculated based on the SEM observation for dry samples, were assumed to be valid for the gold nanoparticles dispersed in the aqueous solution and were utilized to evaluate lectin-induced aggregation of the nanoparticles in the following section. Note that the dynamic light scattering (DLS) measurement of the aqueous dispersion of the PEGylated gold nanoparticles and the bare gold nanoparticles gave the hydrodynamic diameters of 40.9 and 25.1 nm, respectively. Then, the subtraction of the latter from the former yields the PEG thickness in the wet state as 7.9 nm, which is consistent with the value determined by SEM. This negligible discrepancy in the PEG thickness between dry and wet samples may presumably be due to the relatively high density of PEG brushes on the gold surface.

Aggregation of PEGylated Gold Nanoparticles by RCA_{120} Lectin. Figure 3 shows a typical time-dependent change observed in UV–visible spectra of PEGylated gold nanoparticles possessing 65% lactose on the surface (lac65) after the addition of 200 μg/mL RCA_{120}. The surface plasmon band underwent gradual red-shift from 523 nm as the growth of the aggregate occurred through the interaction of RCA_{120} with gold nanoparticles.[3] After 4 h of incubation, macroscopic aggregates were eventually precipitated out from the solution. It is worth noticing that the spectrum underwent a

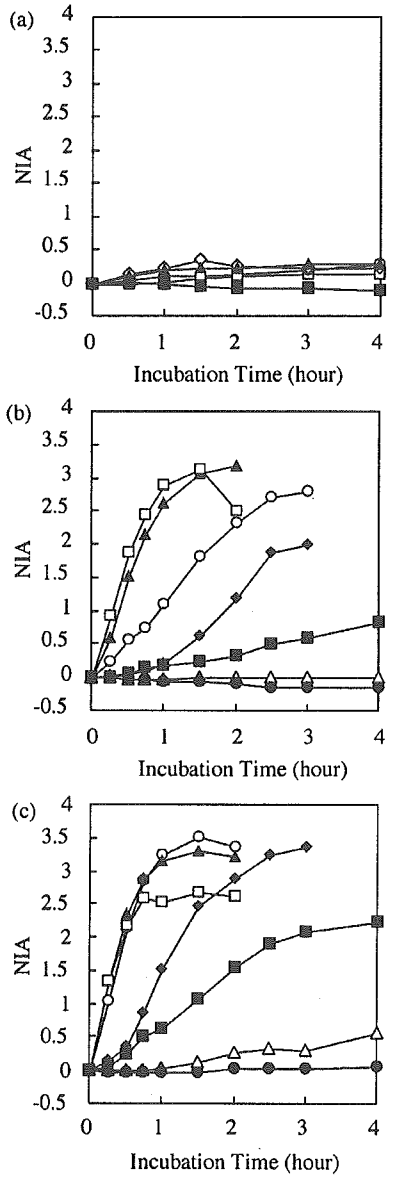

Figure 4. Time-dependent change in normalized integrated absorbance (NIA) of lactose-installed PEGylated gold nanoparticles after the addition of varying concentration of RCA_{120} (●, 10 μg/mL; △, 25 μg/mL; ■, 50 μg/mL; ◆, 100 μg/mL; ○, 200 μg/mL; ▲, 400 μg/mL; □, 800 μg/mL; ◇, 1000 μg/mL). (a) lac20; (b) lac40; and (c) lac65.

complete recovery to the initial profile after the addition of excess amount of galactose (10 mg/mL; Figure 3, dashed line), indicating a redispersion of these PEGylated gold nanoparticles due to the competitive binding of galactose to RCA_{120}. This reversible aggregation-dispersion behavior was further ascertained by TEM (Supporting Information, Figure S2). Note that (acetal-PEG-S-)$_2$-modified gold nanoparticles (lac0) exhibited no change in the spectrum even after the addition of RCA_{120} (Supporting Information, Figure S3), indicating that the lactose-installed PEGylated gold nanoparticles underwent lectin-specific aggregation with negligible nonspecific interaction.

Since the lactose density on the surface is systematically changed for the samples (lac20, lac40, and lac65) depicted

Table 2. Assumed Number of Monovalently bound RCA_{120} Lectin Molecules Per Gold Nanoparticle at Equilibrium Condition (N_b)[a]

lectin conc	10 μg/mL	25 μg/mL	50 μg/mL	100 μg/mL
lac20	0.46	1.1	2.3	4.4
lac40	0.92	2.3	4.5	8.8
lac65	1.5	3.7	7.3	14

[a] N_b is calculated from the equilibrium constant below, assuming the monovalent lectin association with lactose on gold nanoparticles.

$$RCA_{120} + \text{lactose} \rightleftharpoons RCA_{120}\text{-lactose}$$

$$K_a = \frac{[RCA_{120} - \text{lactose}]}{[RCA_{120}][\text{lactose}]} = 2.67 \times 10^4\ M^{-1}\ (25\ °C)$$

in Table 1, a relationship between the sensitivity of lectin-induced aggregation and the lactose density was then evaluated in detail from the normalized integrated absorbance (NIA)[11] between 600 and 750 nm defined in the Experimental Section. There was an obvious increase in NIA with time and lectin concentration dependent manner for lac40 and lac65, indicating the progressive aggregation of gold nanoparticles triggered by lectin (Figure 4, parts b and c). Although lac65 generally revealed higher response than lac40, both became insensitive in the concentration range of lectin lower than the critical value, 25 and 50 μg/mL for lac65 and lac40, respectively. This indicates the presence of critical lectin concentration as to the aggregation of gold nanoparticles. The average number of lectin molecules binding onto a single gold nanoparticle (N_b) at equilibrium condition was calculated, assuming the monovalent association, for varying lectin concentration from the association constant of RCA_{120} lectin and lactose ($K_a = 2.67 \times 10^4\ M^{-1}$ at 25 °C)[16] and was summarized in Table 2. Note that the calculated number of bound lectin molecules in Table 2 is the assumed value based on the monovalent scheme, and thus, the actual number should take a substantially higher value than the calculated one in the region higher than the critical lectin concentration, above which the multivalent binding starts to occur, inducing the lectin-bridged aggregation of nanoparticles. Consequently, the values in Table 2 may only be actual ones in the region under the critical lectin concentration. What we would like to on focus here is that the calculated number of bound lectin molecules (N_b) on a single nanoparticle, based on the assumed monovalent interaction, takes a higher value than 3 in the range of lectin concentration inducing obvious aggregation of lac40 and lac65. The interaction mode may switch from monovalent to multivalent in this range, suggesting the formation of a stable interparticle bridge. Presumably, the binding of more than 3 lectin molecules per particle may be required for the formation of the network of gold nanoparticles large enough to form the macroscopic aggregates. Furthermore, NIA of lac65 and lac40 revealed a proportional increase to lectin concentration in the range of 50~400 and 25~200 μg/mL, respectively (Figure 5), indicating that simple quantification of lectin can be accomplished in the wide concentration range by the use of lactose-installed PEGylated gold nanoparticles with optimized lactose density. A drop of NIA at large RCA_{120} lectin concentration was due to the precipitation of aggregated gold nanoparticles and may not be caused by the saturation of the nanoparticle surface by singly occupied

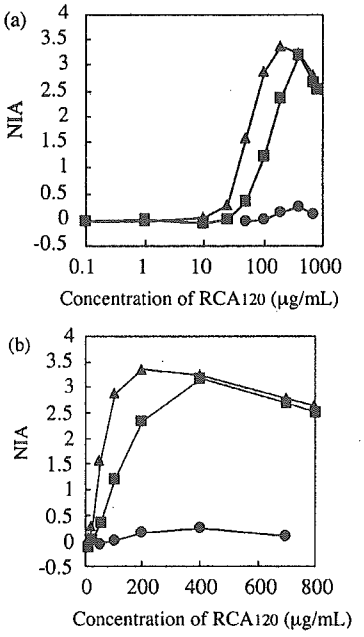

Figure 5. NIA obtained 2 h after the addition of RCA_{120} in varying concentration to the suspension of lactose-installed PEGylated gold nanoparticles (●, lac20; ■, lac40; ▲, lac65). (a) logarithmic scale; (b) linear scale.

RCA_{120} molecules, considering the value of the association constant. Choice of smaller-sized particles with an appropriate ligand density may prevent the precipitation to permit a quantitative aggregation assay in a wider concentration range by the use of lac65 and lac40. On the other hand, lac20 did not undergo lectin-induced aggregation even in the range of lectin concentration (Figure 4a) enough to attain the N_b higher than 3 (>100 μg/mL). It is likely that there exists a critical lactose density on the gold nanoparticles to form lectin-induced aggregates between 20% and 40% of lactose functionality. The area occupied by a single RCA_{120} lectin molecule estimated from its size[17] is 24 (= 6 × 4) nm^2, whereas the area occupied by a single lactose molecule on the particle surface estimated from the number of lactose molecules and the surface area of nanoparticles are 34 and 17 nm^2 for lac20 and lac40, respectively (Table 1). The binding constant of RCA_{120} with lactose is reported to be on the order of 10^4 M^{-1} (see Table 2) and is insufficiently low to form a stable network of lactose-installed gold nanoparticles bridged by a single lectin molecule with divalent functionality. It may be reasonable to assume that more than two lectin molecules may concomitantly participate in the stable interparticle bridge to enhance the association force through multivalent interaction. It is reported that lactose-installed polymeric micelles behave as multivalent ligands for lectins immobilized on a gold surface with an increase in the binding constant of up to 2 orders of magnitude with respect to a monovalent system.[18] Furthermore, Woller and co-workers demonstrated the importance of multivalent interaction, showing that the recognition property of mannose/hydroxyl-functionalized dendrimers against Concanavalin A (Con A) lectin extremely decreased when the area per mannose molecule on the dendrimer surface is more than 17 nm^2.[19] Presumably, lactose density on lac20 may not be high enough to form a multi-molecular bridging structure by RCA_{120}. These results clearly indicate that the regulation of ligand density on the surface of gold nanoparticles is a crucial factor to control the sensitivity of gold colloidal sensors based on the biospecific aggregation.

Conclusions

PEGylated gold nanoparticles possessing a regulated density of lactose (0~65%) on the distal end of PEG were prepared by treating gold colloids with a mixed solution of (lactose-PEG-S-)$_2$ and (acetal-PEG-S-)$_2$ of varying compositions. The number of PEG strands on each particle and average diameter of PEGylated gold nanoparticles were estimated from the results of TGA and SEM measurements, respectively, allowing the lactose density on the surface of PEGylated gold nanoparticles with different lactose functionality to be determined. These PEGylated gold nanoparticles are highly stable under physiological condition, and eventually, those having 65% functionality of lactose (lac65) underwent sensitive RCA_{120} lectin-induced aggregation as well as quantitative re-dispersion with an addition of excess galactose. The shift in the plasmon absorption in UV−visible spectra due to the particle aggregation correlated with the lectin concentration, showing the feasibility of the system as a quantitative assay method. Furthermore, the concentration range of quantitative assay can be modulated by controlling the lactose density on the gold nanoparticles. A critical lactose density (>20%) to trigger lectin-induced aggregation was observed, suggesting that interaction between the nanoparticles may involve a multivalent recognition process. These findings indicate that the optimization of ligand density on the surface of gold nanoparticles as well as the prevention of nonspecific interactions through a steric-repulsive layer of PEG are key factors to construct highly sensitive colloidal biosensor based on the aggregation behavior of gold nanoparticles.

Acknowledgment. The authors express their gratitude to Dr. Yuichi Yamasaki, University of Tokyo, for invaluable advice about image processing. This work was financially supported by the Special Coordination Funds for Promoting Science and Technology from the Ministry of Education, Culture, Sports, Science and Technology of Japan (MEXT), by the Core Research for Evolutional Science and Technology (CREST) from the Japan Science and Technology Agency (JST) and by 21st Century COE Program "Human-Friendly Materials based on Chemistry" from MEXT.

Supporting Information Available. ^1H NMR spectrum of (lactose-PEG-S-)$_2$, TEM images representing the reversible aggregation-dispersion behavior of PEGylated gold nanoparticles, and UV−visible spectra of lac0 after the addition of RCA_{120}. These materials are available free of charge via the Internet at http://pubs.acs.org.

References and Notes

(1) (a) Hirsch, L. R.; Jackson, J. B.; Lee, A.; Halas, N. J.; West, J. L. *Anal. Chem.* **2003**, *75*, 2377−2381. (b) Storhoff, J. J.; Marla, S. S.; Bao, P.; Hagenow, S.; Mehta, H.; Lucas, A.; Garimella, V.; Patno, T.; Buckingham, W.; Cork, W.; Müller, U. R. *Biosens. Bioelectron.*

2004, *19*, 875−883. (c) Haes, A. J.; Van Duyne, R. P. *J. Am. Chem. Soc.* **2002**, *124*, 10596−10604. (d) Zanchet, D.; Micheel, C. M.; Parak, W. J.; Gerion, D.; Alivisatos, A. P. *Nano Lett.* **2001**, *1*, 32−35. (e) Chan, W. C. W.; Nie, S. *Science* **1998**, *281*, 2016−2018.

(2) (a) Taton, T. A.; Mirkin, C. A.; Letsinger, R. L. *Science* **2000**, *289*, 1757−1760. (b) Rosenzweig, Z.; Thanh, N. T. *Anal. Chem.* **2002**, *74*, 1624−1628. (c) Souza, G. R.; Miller, J. H. *J. Am. Chem. Soc.* **2001**, *123*, 6734−6735. (d) Kim, Y.; Johnson, R. C.; Hupp, J. T. *Nano Lett.* **2001**, *1*, 165−167. (e) Daniel M.-C.; Astruc, D. *Chem. Rev.* **2004**, *104*, 293−346. (f) Ishii, T.; Otsuka, H.; Kataoka, K.; Nagasaki, Y. *Langmuir* **2004**, *20*, 561−564.

(3) (a) Takeuchi, Y.; Ida, T.; Kimura, K. *Surf. Rev. Lett.* **1996**, *3*, 1205−1208. (b) Bohren, C. F.; Huffman, D. R. *Adsorption and Scattering of Light by Small Particles*; Wiley: New York, 1983; Chapter 4. (c) Lazaride, A. A.; Schatz, G. C. *J. Phys. Chem. B* **2000**, *104*, 460−467. (d) Kreibig, U.; Genzel, L. *Surf. Sci.* **1985**, 678−700.

(4) Hayat, M. A. *Colloidal Gold: Principles, Methods, and Applications*; Academic Press: San Diego, CA, 1991.

(5) (a) Mangeney, C.; Ferrage, F.; Aujard, I.; Marchi-Artzner, V.; Jullien, L.; Ouari, O.; Rékai, E. D.; Laschewsky, A.; Vikholm, I.; Sadowski, J. W. *J. Am. Chem. Soc.* **2002**, *124*, 5811−5821. (b) McIntosh, C. M.; Esposito, E. A., III.; Boal, A. K.; Simard, J. M.; Martin, C. T.; Rotello, V. M. *J. Am. Chem. Soc.* **2001**, *123*, 7626−7629. (c) Shiraishi, Y.; Arakawa, D.; Toshima, N. *Eur. Phys. J. E* **2002**, *8*, 377−383. (d) Templeton, A. C.; Chen, S.; Gross, S. M.; Murray, R. W. *Langmuir* **1999**, *15*, 66−76.

(6) (a) de la Fuente, J. M.; Barrientos, A. G.; Rojas, T. C.; Rojo, J.; Canada, J.; Fernández, A.; Penadés, S. *Angew. Chem., Int. Ed.* **2001**, *40*, 2257−2261. (b) Berrientos, Á. G.; de la Fuente, J. M.; Rojas, T. C.; Fernández, A.; Penadés S. *Chem. Eur. J.* **2003**, *9*, 1909−1921.

(7) Akiyama, Y.; Otsuka, H.; Nagasaki, Y.; Kato, M.; Kataoka, K. *Bioconjugate Chem.* **2000**, *11*, 947−950.

(8) Otsuka, H.; Akiyama, Y.; Nagasaki, Y.; Kataoka, K. *J. Am. Chem. Soc.* **2001**, *123*, 8226−8230.

(9) Mammen, M.; Choi, S.; Whitesides, G. *Angew. Chem., Int. Ed. Engl.* **1998**, *37*, 2754−2794.

(10) Fantuzzi. G.; Pengo, P.; Gomila, R.; Ballester, P.; Hunter, A. C.; Pasquato, L.; Scrimin, P. *Chem. Commun.* **2003**, 1004−1005.

(11) Nath, N.; Chilkoti, A. *J. Am. Chem. Soc.* **2001**, *123*, 8197−8202.

(12) NIH image was developed at the National Institutes of Health, USA and is available from the Internet by anonymous FTP from zippy.nimh.nih.gov.

(13) Walker, C. H.; St. John, J. V.; Wisian-Neilson, P. *J. Am. Chem. Soc.* **2001**, *123*, 3846−3847.

(14) Tanford, C.; Nozaki, Y.; Rohde, M. F. *J. Phys. Chem.* **1977**, *81*, 1555−1560.

(15) Flory, P. J. *Statistical Mechanics of Chain Molecules*; Wiley: New York, 1969; Chapter I and V.

(16) Dooley, T. P.; Houston, L. L. *J. Biol. Chem.* **1982**, *257*, 4147−4151.

(17) Sweeney, E. C.; Tonevitsky, A. G.; Temiakov, D. E.; Agapov, I. I.; Saward, S.; Palmer R. A. *Proteins* **1997**, *28*, 586−589.

(18) Jule, E.; Nagasaki, Y.; Kataoka, K. *Bioconjugate Chem.* **2003**, *14*, 177−186.

(19) Woller, E. K.; Walter, E. D.; Morgan, J. R.; Singel, D. J.; Cloninger, M. J. *J. Am. Chem. Soc.* **2003**, *125*, 8820−8826.

BM049427E

Preparation and Biological Characterization of Polymeric Micelle Drug Carriers with Intracellular pH-Triggered Drug Release Property: Tumor Permeability, Controlled Subcellular Drug Distribution, and Enhanced in Vivo Antitumor Efficacy

Younsoo Bae,[†] Nobuhiro Nishiyama,[‡] Shigeto Fukushima,[†] Hiroyuki Koyama,[‡] Matsumura Yasuhiro,[§] and Kazunori Kataoka*,[†]

Department of Materials Science and Engineering, Graduate School of Engineering, The University of Tokyo, 7-3-1 Hongo, Bunkyo-ku, Tokyo 113-8656, Japan, Department of Clinical Vascular Regeneration, Graduate School of Medicine, The University of Tokyo, 7-3-1 Hongo, Bunkyo-ku, Tokyo 113-8655, Japan, and Investigative Treatment Division, National Cancer Center Research Institute East, 6-5-1 Kashiwanoha, Kashiwa, Chiba 277-8577, Japan. Received July 28, 2004; Revised Manuscript Received October 31, 2004

A novel intracellular pH-sensitive polymeric micelle drug carrier that controls the systemic, local, and subcellular distributions of pharmacologically active drugs has been developed in this study. The micelles were prepared from self-assembling amphiphilic block copolymers, poly(ethylene glycol)-poly(aspartate hydrazone adriamycin), in which the anticancer drug, adriamycin, was conjugated to the hydrophobic segments through acid-sensitive hydrazone linkers. By this polymer design, the micelles can stably preserve drugs under physiological conditions (pH 7.4) and selectively release them by sensing the intracellular pH decrease in endosomes and lysosomes (pH 5–6). In vitro and in vivo studies show that the micelles have the characteristic properties, such as an intracellular pH-triggered drug release capability, tumor-infiltrating permeability, and effective antitumor activity with extremely low toxicity. The acquired experimental data clearly elucidate that the optimization of both the functional and structural features of polymeric micelles provides a promising formulation not only for the development of intracellular environment-sensitive supramolecular devices for cancer therapeutic applications but also for the future treatment of intractable cancers with limited vasculature.

INTRODUCTION

The selective augmentation of drug concentrations in avascular tumor tissues is the most challenging issue of current cancer chemotherapy using macromolecular bioconjugates (*1–3*). Most anticancer drugs are pharmacologically effective but limited in their clinical applications due to serious toxicity and low water solubility; thereby, the altered biodistribution of these drugs has an important meaning not only to reduce the toxicity but also to improve therapeutic effects (*4–6*). For these reasons, interest has centered on the creation of drug carriers that safely and precisely deliver the appropriate amounts of active drugs to solid tumors (*7–10*). Indeed, several macromolecular drug carriers are under clinical trials or used practically, which include water-soluble polymer–drug conjugates (*11*), liposomal carriers (*12*), and polymeric micelles (*13*). However, even though these carriers have made significant advancements in cancer therapy, recent studies point out their antitumor activities are subject to change according to the cancer species with pathological, pharmacological, and biochemical differences (*14*).

There are three major reasons why the present macromolecular drug carriers have difficulties in clinical use. First, the carriers injected into the body encounter in vivo barriers such as nonspecific systemic accumulation and phagocytotic clearance by the host defense system (*15*). Second, even after the carriers accumulated in solid tumors avoiding these in vivo barriers, they still have to overcome the heterogeneous tumor microenvironments that are characterized by insufficient blood supply, disordered vasculatures, and diffusion-limited interstitum (*16*). Third, the carriers that successfully accessed the inside of tumor tissues should release the loaded drugs back into active forms in order to exert the antitumor effect (*17*). Among these reasons, poor permeability of the carriers inside the tumor tissues and low concentrations of active drugs throughout solid tumors become particularly serious problems (*18, 19*). For these reasons, understanding the correlation between the physicochemical properties of drug carriers and their behaviors in the body is very important, and the combination of these two features is required for the design of ultimate carriers (*20*).

In this article, we will report that such tantalizing problems may be overcome by a novel tumor-infiltrating drug carrier, the pH-sensitive polymeric micelle, whose structural and functional features were optimized for the intracellular drug delivery (Figure 1A). The micelle is a nanosized supramolecular assembly from the self-assembling amphiphilic block copolymers, poly(ethylene glycol)-poly(aspartate hydrazone adriamycin) [PEG-p(Asp-Hyd-ADR)]. The anticancer drug, adriamycin (ADR), is

* To whom correspondence should be addressed. Phone: +81-3-5841-7138, Fax: +81-3-5841-7139, E-mail: kataoka@bmw.t.u-tokyo.ac.jp.

[†] Department of Materials Science and Engineering, The University of Tokyo.

[‡] Department of Clinical Vascular Regeneration, The University of Tokyo.

[§] National Cancer Center Research Institute East.

10.1021/bc0498166 CCC: $30.25 © 2005 American Chemical Society
Published on Web 12/22/2004

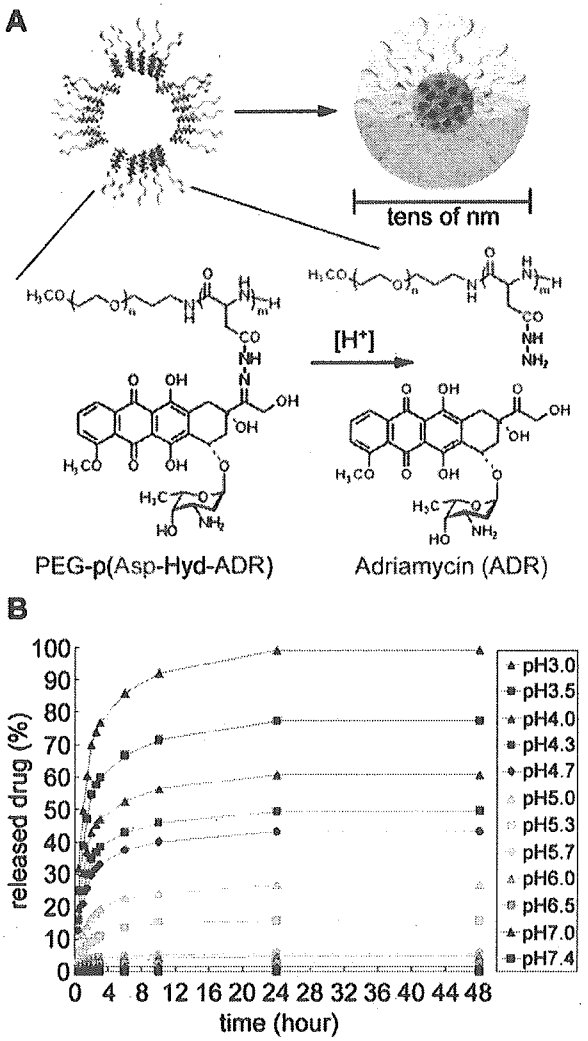

Figure 1. Preparation of tumor-infiltrating polymeric micelles with intracellular pH-sensitivity. (A) Micelles with tens of nm size diameter were prepared from self-assembling amphiphilic block copolymers, PEG-p(Asp-Hyd-ADR), in which the anticancer drug, adriamycin (ADR), was conjugated through acid-sensitive hydrazone linkers. (B) The micelles released the loaded drugs under acidic conditions below pH 6.0 corresponding to intracellular space, but remained stable under the conditions of vascular and extracellular space (pH 7.4–7.0).

conjugated to the core-forming segments through the hydrazone linkers that are stable under physiological conditions (pH 7.4) but cleavable under acidic intracellular environments in endosomes and lysosomes (pH 5–6). This carrier design allows the micelle to safely protect hydrophobic drugs from the host defense system in the body and to selectively exert cytotoxicity due to intracellular pH-triggered drug release, improving both the delivery effect and therapeutic efficacy of the drugs (*21*). Therefore, the characteristic in vitro and in vivo behaviors of the micelles would offer intriguing information taking into account the future design and development of bioresponsive supramolecular carrier systems for the intracellular trafficking of biologically active molecules.

EXPERIMENTAL PROCEDURES

Materials. β-Benzyl-L-aspartate was from Sigma and α-methoxy-ω-amino poly(ethylene glycol) (PEG; MW = 12 000) was from Nippon Oil & Fats, Japan. PEG was purified using an ion-exchange gel column (CM-Sephadex C-50, Amersham Pharmacia Biotech) prior to the synthesis of the block copolymers. Adriamycin hydrochloride-(ADR–HCl) was from Nippon Kayaku, Japan, and its purity was checked by reversed phase liquid chromatograpy (RPLC). Sephadex LH-20 gel was from Amersham Pharmacia Biotech, Sweden.

Cell Lines and Animals. A human small cell lung cancer cell line SBC-3 and murine colon adenocarcinoma 26 (C26) cells were from the National Cancer Center Research Institute, Japan, and cultured in a medium (DMEM, Sigma, St. Louis, MO) containing 10% fetal bovine serum in a humidified atmosphere with 5% CO_2 at 37 °C. CDF-1 mice (female, 6 weeks old) were from Charles River, Japan. The animals were cared for and all experiments were performed in compliance with the Guide for the Care and Use of Laboratory Animals as adopted and promulgated by the National Institutes of Health.

Preparation of the pH-Sensitive Polymeric Micelles. The self-assembling amphiphilic block copolymer, PEG-p(Asp-Hyd-ADR), was synthesized as reported elsewhere (*22*). Briefly, poly(ethylene glycol)-poly(β-benzyl-L-aspartate) (PEG-PBLA) was synthesized from the ring-opening polymerization of β-benzyl-L-aspartate *N*-carboxyanhydride using PEG as a macro initiator, followed by substitution of the benzyl groups of PEG-PBLA with hydrazide groups for drug binding (see also Supporting Information). Unbound ADR was completely removed using Sephadex LH-20 gel, and the obtained polymers were redissolved in dimethylacetamide to prepare the micelle by a dialysis method.

Evaluation of Acid-Sensitive Drug Release from the Micelles. Reversed phase liquid chromatograpy (RPLC) analysis, using a μ-Bondasphere 5 μm C4-300A column (Nihon Waters, Japan), was used to assess the pH sensitivity of the micelle. The micelle with a 10 mg/mL concentration was incubated under various buffered conditions from pH 7.4 to 3.0 [20 mM phosphate buffer (pH 7.4–6.0), 20 mM acetate buffer (pH 5.8–3.0)], and time- and pH-dependently released drugs were measured from the peak intensity by a UV detector (485 nm).

Observations on Intracellular Drug Release and Localization of the Micelles. Multicellular tumor spheroid (MCTS) was prepared from a C26 cell line using a spheroid culture plate, Sumiloncelltight (Sumitomo Bakelite, Japan); 200 μm size MCTS were sorted and used for the experiments. Fluorescence images were observed using a confocal laser scanning microscope (LSM 510, Carl Zeiss, Germany) with a 20× objective (Plan-Apochromat, Carl Zeiss, Germany) and a 63× objective (C-Apochromat, Carl Zeiss, Germany) at excitation wavelengths of 488 nm (Ar laser) and 364 nm (UV laser) for ADR and Hoechst 33258, respectively. The concentrations of the micelles in the medium were adjusted to 10 μg/mL (ADR equivalent). All images were acquired and processed with the accompanying software.

In Vitro Growth Inhibition Assay. A tetrazolium dye method, called the MTT assay, was used to evaluate the growth-inhibitory effect of the micelle. Using 96-well culture plates, exponentially growing SBC-3 cells were seeded (2000 cell/well) and preincubated for 24 h, followed by coincubation with ADR and the micelle samples. After exposure for 3, 10, and 24 h, the medium was discarded and each cell was reincubated in fresh medium for another 24 h. The cells were then counted using a Bio-RAD Microplate Reader 550 (Bio-Rad Laboratories Inc.).

In Vivo Antitumor Activity and Body Weight Change of Mice. The antitumor activity of the micelles was evaluated with tumor bearing, 7-week-old, female SPF CDF1 mice (n = 6, Charles River, Japan). After implanting C26 cells 10 days earlier, injection of the samples took place using a volume of 0.1 mL/10 g body weight. The regimens of the micelles were scheduled by changing the administration dose (20, 40, and 60 mg/kg) three times with a 4-day interval, based on the optimized regimens of ADR as a control. However, in the case of ADR, only limited doses (5, 10, and 15 mg/kg) were applied to the mice due to the drugs toxicity. The mice were monitored daily, and tumor growth and body weights were measured at 2-day intervals. Tumor volume is calculated as follows: volume = $1/2 \times LW^2$ (L is the long diameter and W is the short diameter of a tumor).

Biodistribution and Pharmacokinetics. The CDF1 mice (n = 6), when the tumor volume reached ca. 100 mm^3, were injected with ADR and the micelles in a volume of 0.1 mL/10 g body weight for the experiments. The dose was either 10 mg/kg for ADR or the micelles (ADR equivalent). After the injection, blood, tumor, and major organs (heart, kidney, liver and spleen) were collected at 0.5, 1, 3, 6, 9, 24, and 48 h, followed by HPLC anaylsis (see Supporting Information for the detailed protocol).

Fluorescence Microscopic Observations of Solid Tumors and Their Peripheral Blood Vessels. The tumor-bearing mice were sacrificed at 24 h after the injection of the micelles with a 10 mg/kg dose. The intact tumor tissues with their peripheral blood vessels were harvested for macroscopic observations using a fluorescence microscope (Axiovert 200, Carl Zeiss, Germany) equipped with a 2.5× objective (Plan-Neofluar, Carl Zeiss, Germany) and a filter set15 (BP546/12, FT580, LP590, mercury lamp excitation, Carl Zeiss, Germany).

RESULTS

Preparation of the Intracellular pH-Sensitive Polymeric Micelles. The polymer backbone of PEG-p(Asp-Hyd-ADR) consisted of poly(ethylene glycol) (PEG) with a molecular weight of 12 000 g/mol for the hydrophilic shell-forming segment and 37 repeating units of polyaspartate (PAsp) for the core-forming segment (MW = 28 679), which were determined by gel permeation chromatography and ^{1}H NMR measurements. The 28 side chains in the PAsp block were replaced by hydrazide groups for the binding of the drugs. Adriamycin (ADR) was then conjugated to the polymer backbone through hydrazone bonds between the carbonyls at the C13 of ADR and the hydrazide groups of the PEG-p(Asp-Hyd) block copolymer. Even though the biological and chemical background of binding ADR to polymer backbone through hydrazone linkages has been delineated in our previous work (*22*) as well as many studies (*23*–*26*), it must be noticed that the hydrazone linkage is the most popularly used as pH-sensitive linkers due to the fact that this bond is quite stable at pH 7.4 but hydrolyzes under mild acidic conditions with pH 5–6. Therefore, to ensure that drug release from the micelles occurs only when acid-labile hydrazone linkers are cleaved, any unbound free ADR were completely removed in this study. These were confirmed by a reversed phase liquid chromatograpy (RPLC) analysis that is generally used for separating and purifying materials due to the differences in their hydrophobic properties (further details are described below). RPLC analysis showed the drug loading content of PEG-p(Asp-Hyd-ADR) was 42.5 wt % with respect to a single block copolymer chain. The obtained PEG-p(Asp-Hyd-ADR) block copolymers self-assembled into micelles in aqueous solutions; the prepared micelles had a 65 nm diameter, which was confirmed by dynamic light scattering measurements.

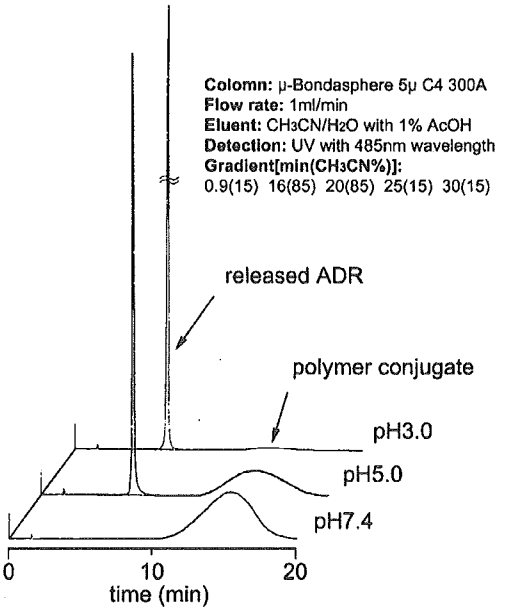

Figure 2. Acid-sensitive cleavage of drug-binding hydrazone bonds evaluated by reversed phase liquid chromatography (RPLC) analysis. RPLC separates free drugs and polymer conjugates due to the differences in their hydrophobic properties, demonstrating absence of free drugs at pH 7.4 possibly binding to polymer conjugates in a physical way. On the other hand, it clearly shows that the amount of released drugs increases under acidic conditions in which the drug-binding hydrazone linkers can be cleaved.

The Micelles Selectively Release the Loaded Drugs by Sensing a pH Decrease. To confirm the acid-sensitive drug release profile, the micelles were incubated under various pH conditions from 7.4 to 3.0, and the released drugs were measured using RPLC analysis. Figure 1B shows that the micelles released the loaded drugs time- and pH-dependently as the external pH decreased, while they were stable under physiological conditions at pH 7.4 for over 48 h. The results indicate the micelles should release the loaded drugs in the intracellular acidic regions (pH 5–6) such as endosomes and lysosomes in which the drug-binding hydrazone linkers can be cleaved most effectively. Chemical evidence for absence of free drugs and acid-sensitive cleavage of hydrazone linkers to induce drug release was also presented by RPLC analysis (Figure 2). As described above, ADR is conjugated to amphiphilic block copolymers through pH-sensitive hydrazone linkers. If the drugs were simply entrapped in the micelles by physical interaction instead binding to polymers via chemical linkers, a sharp peak corresponding to the free drug should be separated from drug–polymer conjugates by RPLC and appeared in the physiological condition (pH 7.4) where the acid-labile hydrazone bond remains stable. However, the peak from the free drug was not shown at pH 7.4 but gradually increased in acidic conditions while the broad peak from polymer conjugates decreased. Eventually, almost 100% of the drugs were released at pH 3.0, and on the basis of this, we calculated the drug loading content of polymer conjugate described above. These results demonstrate that acid-sensitive cleavage

Table 1. Growth Inhibitory Effects of the Micelles against Cancer Cells[a]

sample	exposure time (hour)	IC_{50}[b] (μg/mL±SD)	relative index[c]
ADR	3	0.041 ± 0.035	1.05
	10	0.048 ± 0.026	1.23
	24	0.039 ± 0.025	1
micelle	3	1.08 ± 0.12	27.69
	10	0.45 ± 0.061	11.54
	24	0.27 ± 0.038	6.92

[a] Eight independent experiments were carried out using a human small cell lung cancer cell line SBC-3 (n = 8). [b] IC_{50} denotes the inhibitory concentration of the drugs required for 50% reduction in cell population. Concentrations of the micelles are calculated with free ADR equivalents. [c] Relative index denotes the ratio between a control and the object for comparison. Here, we evaluated the growth inhibitory effect of the micelles by converting their concentrations with respect to ADR after a 24 h incubation as the control.

of hydrazone linkers between drugs and polymer chains obviously induced drug release.

Regenerated Drugs Were Pharmaceutically Active Inhibiting Cell Growth in Vitro. To verify whether the released drugs are pharmacologically active, an in vitro growth-inhibition test was carried out. The test revealed that the cytotoxic activity of the micelles was as high as 1/7-fold with respect to that of the free drugs after a 24 h exposure time (Table 1). Interestingly, the micelles showed delayed cytotoxicity that was drastically changed depending on the incubation time, which reflects that the drug release from the micelles took place and correlated with the cell metabolism.

The Micelle Infiltrates into the Avascular Tumor Model Multicellular Tumor Spheroids. Recently, it has been reported that the fluorescence quenching effect of the micelles provides a useful tool to observe the intracellular behaviors of the micelles (*22*). The fluorescence intensity of ADR, playing a role not only as an anticancer drug, but also as a fluorescence probe in this study, is quenched due to the locally increased high concentration in the micelle core; however, the fluorescence becomes detectable again as the micelles start to release ADR under acidic conditions. Consequently, the micelles emit intense fluorescence signals with the release of the entrapped ADR; a series of processes such as intracellular trafficking, drug release, and localization were able to be directly monitored in live cells accompanying the structural change. In the meantime, the multicellular tumor spheroid (MCTS) was used as an in vitro tumor model for the experiments because it is the most similar to avascular tumor regions of practical solid tumors in vivo that are characterized by limited accessibility of cell subpopulations (Figure 3). For example, MCTS reproduces adverse microenvironmental conditions of solid tumors in vivo such as hypoxia and nutritional depletion, and the extracellular matrix between tumor cells instead of intratumoral normal cell populations (*27*–*28*).

For these reasons, the intracellular behaviors of the micelles were observed within solid tumors using fluorescence quenching effect and the MCTS. The micelles were coincubated with the MCTS, and the change in the fluorescence intensity was monitored using a confocal laser scanning microscope (CLSM). The three-dimensional CLSM images demonstrated the time-dependent change in the fluorescence intensity of the micelle systems and their distributions throughout the MCTS with a 200 μm diameter depending on the incubation time (Figure 4A). The 200 μm diameter of MCTS was

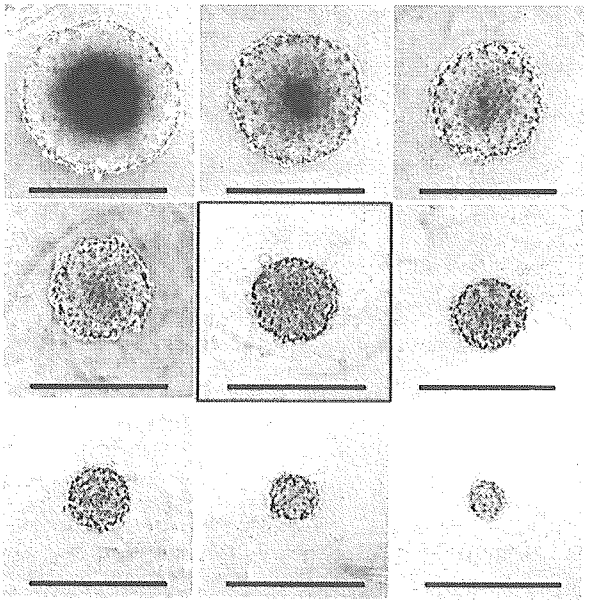

Figure 3. Preparation of multicellular tumor spheroid (MCTS). MCTS with diameter ranging from 100 to 500 μm was prepared from a C26 cell line. Among them, MCTS with a 200 μm diameter (red-edged) was used as an in vitro tumor model because it has the most suitable size for reproducing in vivo avascular tumor regions that are characterized by limited accessibility of cell subpopulations (bar = 500 μm).

determined as the most suitable size for the experiments, considering the fact that the maximum distance between the capillary blood vessels within avascular solid tumor is 200 μm or less (*29*). The fluorescence of the micelle system remained quenched at 1 h after incubation, but it was detected at 3 and 24 h. It is notable that most cell nuclei remained blue at 3 h. The images, therefore, suggest that the micelles began to intracellularly release the drugs but the released drugs were still localized in the cytoplasm. However, the intense fluorescence of ADR was eventually detected in most of the cell nuclei after 24 h. These results reflect that the micelles would access every cell in the avascular region of tumor tissues in vivo to release the drugs.

The Micelles Enter the Cell Interior and Release the Drugs. To get a better understanding of the intracellular distributions of the micelles and their released drugs, further observations of the MCTS coincubated with the micelles under high magnification were carried out using a 63× objective (Figure 4B). These images show clear evidence of the intracellular drug release from the micelles and accumulation of the released drugs in the cell nuclei. The localization of the ADR fluorescence in the cytoplasm after 3 h incubation is supporting our speculation that the micelles internalized the cells releasing the drugs. After additional incubation up to 24 h, the presence of the drugs both in the cytoplasm and cell nuclei was confirmed. When the same experiments were carried out with free ADR, all the cell nuclei in the MCTS became red within 1 h because the ADR with a low molecular weight rapidly penetrated into each cell, and we were not able to observe this unique time-dependent fluorescence change in intensity and its distribution. Therefore, it is obvious that the micelles are precisely functioning in the intracellular regions as we designed, and the possible drug release from the micelles in the extracellular regions is negligible.

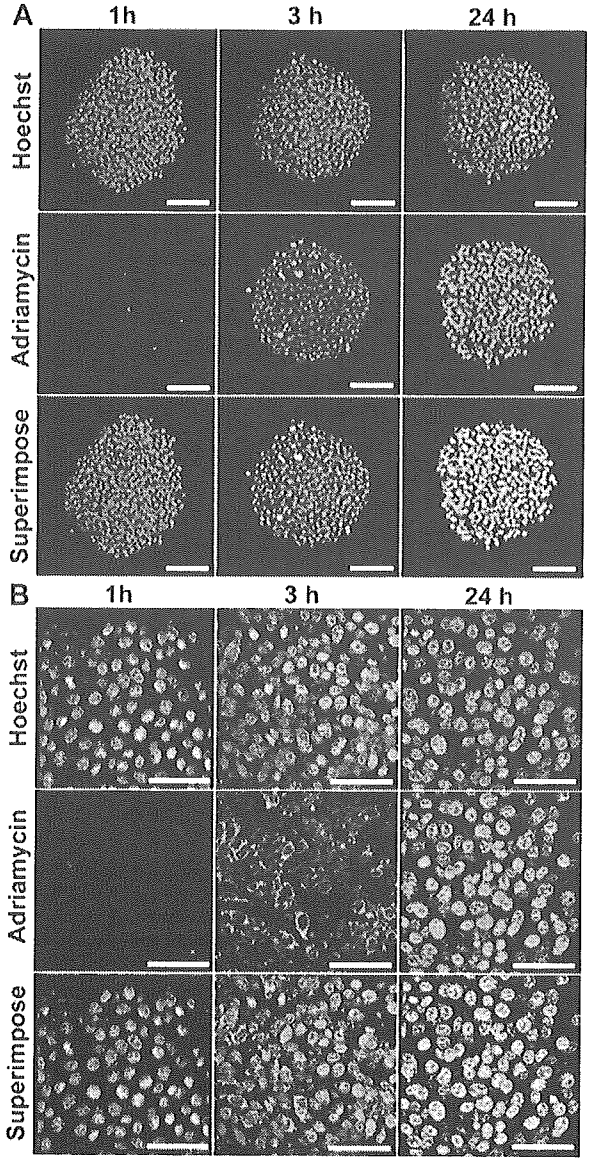

Figure 4. Observation of tumor permeability and intracellular drug release behaviors of the micelles. (A) CLSM observations showed the time-dependent change in the fluorescence intensities of ADR in the micelle system in MCTS. The images showed that the micelles can access the inside of the MCTS and release the loaded drugs (bar = 100 μm). (B) The intracellular drug release and localization of the micelles in each cell of MCTS were observed in detail using a high-magnification 63× objective. The images clearly demonstrated that the micelles internalized into the cells and released drugs, and that the released drugs eventually accumulated in the cell nuclei (bar = 50 μm).

The Micelles Suppress Tumor Growth in Mice with Enhanced Therapeutic Efficacy and Lowered Toxicity. The animal tests revealed that the micelles exerted an effective antitumor activity over a broad range of injection doses to suppress tumor growth in mice, showing some of the clear comparisons with ADR (Figure 5). In the case of ADR, tumor growth was suppressed with a 10 mg/kg dose, but the mice treated with a 15 mg/kg dose were dead due to the drug's toxicity. This corresponds well to the fact that the lethal dose of ADR killing 50% of the test animals within a designated period, called LD_{50}, is generally 12.7−13.2 mg/kg. On the contrary, the micelles were safely injectable up to a 40 mg/kg dose, while three of six mice were completely cured and there was no death among the treated mice. Notably, the body weights of the mice that slightly decreased during the micelle administration recovered, or even increased, on day 30 with respect to the controls (Table 2). Such behavior was not observed in the case of ADR, and the mice were emaciated with a 10 mg/kg dose that was the optimum dose for ADR to suppress tumor growth. Namely, the therapeutic efficacy of the micelles was significantly improved over that of ADR within this animal experiment setting, which distinguishes the micelles from ADR that has a narrow therapeutic window between 10 and 15 mg/kg. In the meantime, the tumor-suppressing antitumor activity of the micelles is shown from a 20 mg/kg dose. The micelles also extended the duration of tumor growth reaching a 5-fold initial tumor volume up to 22 and 28 days for the 20 and 40 mg/kg doses, respectively. These results indicate that the micelles achieved both enhanced therapeutic efficacy and a reduced toxicity of the loaded drugs, which are of great advantage to create effective and safe drug carrier systems.

Table 2. In Vivo Antitumor Activity of the Micelles against C26 Tumor-Bearing Mice

sample	dose (mg/kg)[a]	body weight change on day 30 (%)[b]	toxic death	duration days of tumor growth[c]	complete cure
control	0	−2.18 ± 1.74	0/6	3.7	0/6
ADR	5	−13.35 ± 0.59	0/6	4.2	0/6
	10	−16.84 ± 1.26	0/6	14.6	1/6
	15	–	6/6	–	–
micelle	5	−0.89 ± 1.68	0/6	3.9	0/6
	10	−4.51 ± 1.44	0/6	4.0	0/6
	20	3.13 ± 1.60	0/6	22.1	2/6
	40	−4.07 ± 0.92	0/6	27.9	3/6
	60	–	6/6	–	–

[a] Administrations were carried out three times with a 4-day interval, and doses were determined in free ADR equivalents. [b] Body weights were measured on day 30 after the first injection to compare the long-term toxicity between ADR and the micelles. Values are expressed as mean ± SEM. [c] Duration time to reach 5-fold initial tumor volume.

The Micelles Circulate for a Long Time in the Blood and Selectively Accumulate in Solid Tumors. Effective antitumor activity and low toxicity imply that the micelles are stable in the blood without drug release (or leakage); therefore, their systemic and local distribution may dominate the tumor-suppressing antitumor activity. To demonstrate this, we investigated the in vivo dispositions of the micelles in detail using a biodistribution study. The levels of the micelles in the blood, tumor, and major organs, such as the heart, kidney, liver, and spleen, are expressed as percentage of each dose at specific times after the intravenous injection (Figure 6A). As summarized in Table 3, the micelles circulated in the blood for a prolonged time, and the area under the concentration curve (AUC) of the blood was 15-fold greater than that of ADR. In particular, it is noteworthy that the AUC values of the micelles in the heart and kidney decreased as compared to ADR, indicating that their tumor selectivity (AUC_{tumor}/AUC_{organ}) increased 6- and 5-fold higher with respect to the heart and the kidney, respectively. Such tumor-selective accumulation of the micelles may reduce the side effects of ADR such as cardiotoxicity and nephrotoxicity. In the meantime, the micelles showed a relatively low uptake in the liver and spleen despite the long residence time in the blood in comparison with tumors. These results suggest that the micelles may rapidly evacuate from these reticular

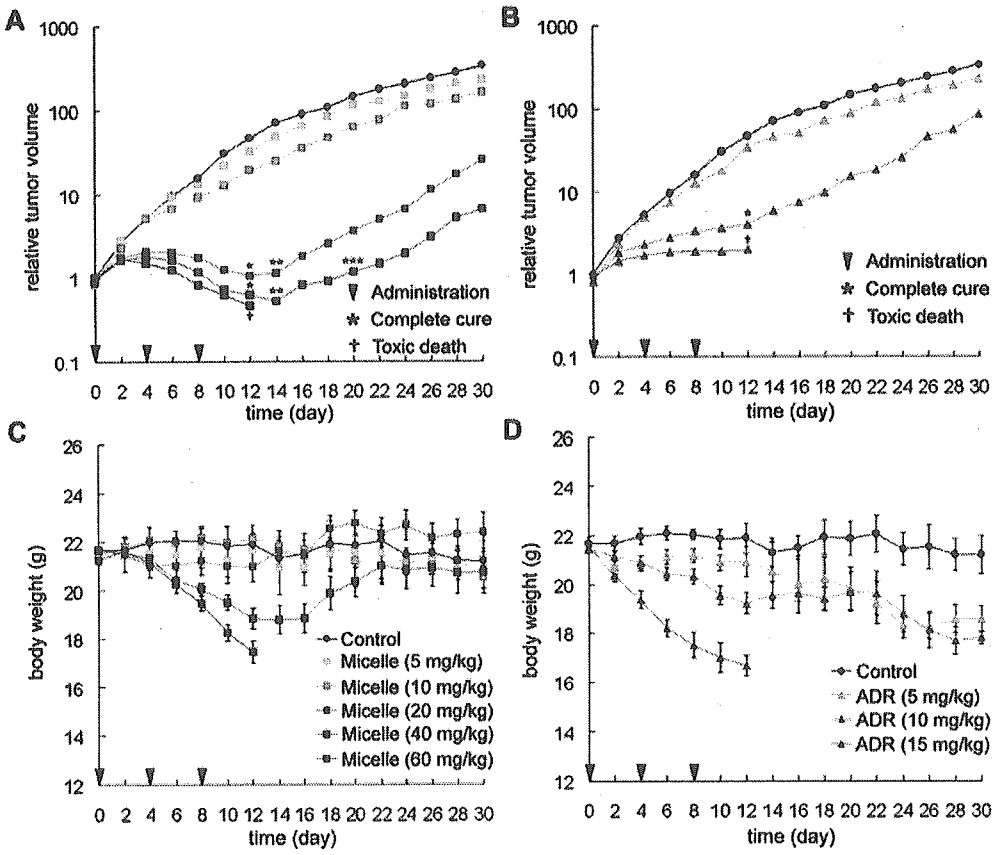

Figure 5. Tumor size and body weight changes of the treated mice. The figures show effective tumor-suppressing activity and low change in body weights over a broad range of injection doses of the micelles (A and C). To the contrary, ADR showed a narrow therapeutic window between 10 and 15 mg/kg does avoiding toxic death (B and D). Administrations were carried out three times with a 4-day interval into tumor bearing CDF1 mice (female, 6-week-old, $n = 6$). The micelle doses are shown as ADR equivalents. Values are expressed as mean and mean ± SEM for the tumor volume and body weight, respectively.

connective tissues without interacting with monocytes and macrophages that are responsible for engulfing and removing cellular debris, old cells, and unwelcome external invaders from the bloodstream. On the contrary, tumor tissues are characterized by a large vascular permeability and high interstitial diffusivity while a lack of lymphatic drainage is observed. This phenomenon is explained by the enhanced permeability and retention (EPR) effect, which significantly affects distributions of the macromolecules facilitating their access and accumulation in tumors (*30, 31*). Consequently, the micelles that accumulated in the solid tumors through the EPR effect can stay for a prolonged time. The biodistribution study, therefore, showed that the cytotoxicity of the micelles seems to depend on their retention time as well as in the accumulated amounts in each organ, which may be crucial in attaining both an effective antitumor activity and reduced toxicity in a single drug carrier system.

In vivo antitumor activity test showed that the micelles effectively suppressed tumor growth in mice over a broad range of injection doses while toxicity remained extremely low. On the other hand, the biodistribution study revealed that the micelles circulated in the blood for a long period of time and accumulated in normal organs as well as the tumors. These results are very interesting because the micelles showed organ-dependent differences in cytotoxicity. To elucidate this, we investigated the localization of the micelles in each organ by calculating the tissue-to-blood concentration ratio K_b (Table 4). The K_b value is defined as $[K_b = C_{tissue}/C_{blood}]$ where C_{tissue} and C_{blood} denote the tissue concentration and the blood concentration of the micelles, respectively. Each K_b value indicates distribution of the micelles in vascular space ($K_b < 0.1$), extracellular space ($0.1 < K_b < 0.5$), and intracellular space ($0.5 < K_b$) (*32, 33*). The data revealed that the micelles localized in the cell interior of tumor tissues but mainly distributed in the extracellular space of other organs after accumulation. It is in good accordance with our previous results published elsewhere (*34, 35*). We speculate that such drastic alterations might be due to the pathological differences in vasculatures and lymphatic drainages between organs. Consequently, even though the micelles accumulate in normal organs, they can be excreted from the body before releasing drugs. The organ-dependent cytotoxicity of the micelles, therefore, probably would depend on their retention time as well as the accumulated amounts in each organ.

The Micelles Regulate the Local Drug Distribution within Solid Tumors. In view of their tumor-specific accumulation and intracellular distribution, the micelles should release the drugs in solid tumors along with emitting fluorescence as we observed in the intracellular drug release experiment using MCTS. In contrast, if the micelles released the drugs slowly or not at all, the fluorescence of ADR would remain quenched. On the basis of this hypothesis, we observed the solid tumors and their peripheral blood vessels in mice after intravenous injection of the micelles using a fluorescence microscope (Figure 6B). The observations were carried out at 24 h after injection because the micelles needed to

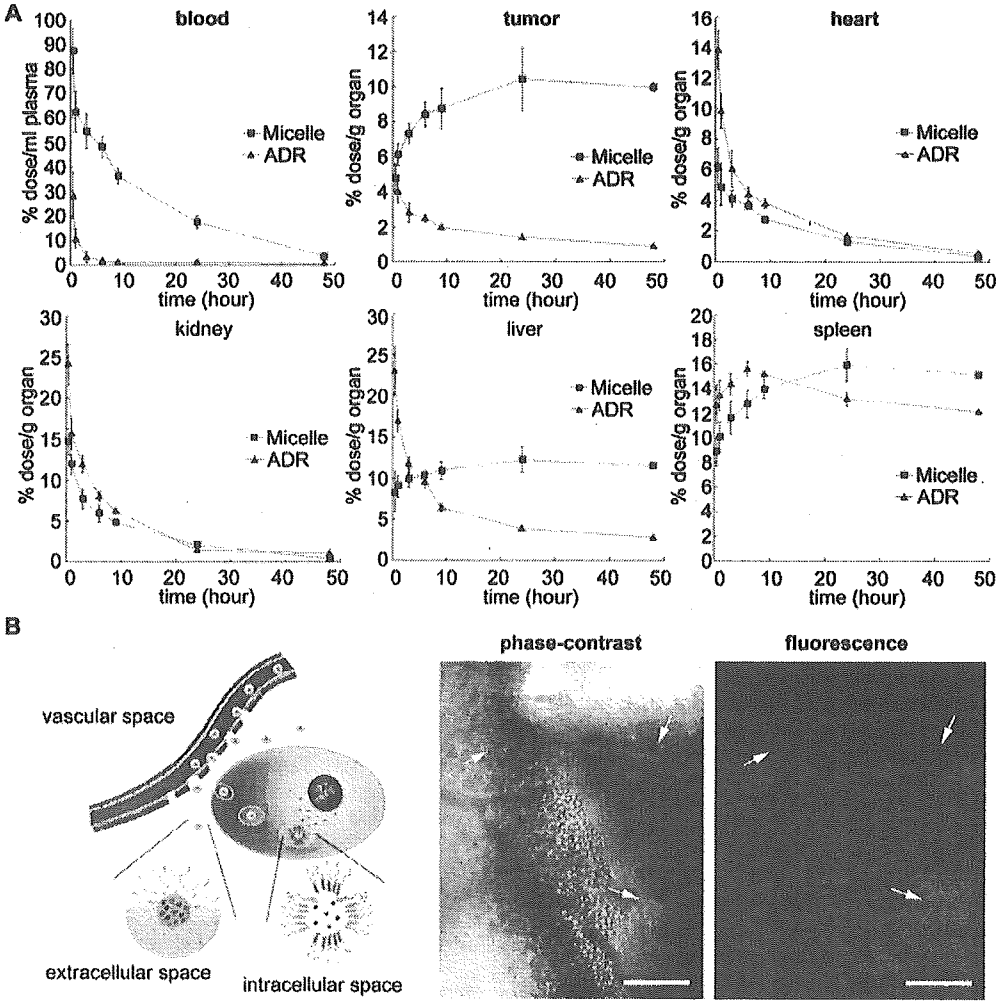

Figure 6. Tumor-specific accumulation of the micelles and locally increased drug concentrations. (A) Biodistribution study revealed the prolonged circulation in the blood and tumor-specific accumulation of the micelles. (B) Fluorescence microscopic observations of the solid tumor and its peripheral regions at 24 h after micelle injection demonstrate that the drug concentrations in the tumor tissues selectively increased due to the tumor-specific accumulation and controlled drug release from the micelles (bar = 500 μm).

Table 3. Tumor-Specific Accumulation of the Micelles

	AUC[a]		AUC ratio ($AUC_{micelle}/AUC_{ADR}$)	tumor selectivity[b] (AUC_{tumor}/AUC_{organ})		tumor selectivity ratio [$(AUC_{tumor}/AUC_{organ})_{micelle}$/ $(AUC_{tumor}/AUC_{organ})_{ADR}$]
	ADR	micelle		ADR	micelle	
blood	58.86	858.54	14.59	–	–	–
tumor	49.59	210.21	4.24	–	–	–
heart	94.70	65.24	0.69	0.52	3.22	6.19
kidney	151.56	117.80	0.78	0.33	1.78	5.39
liver	176.15	261.17	1.48	0.28	0.80	2.86
spleen	341.38	329.66	0.97	0.15	0.64	4.27

[a] AUC denotes the area under a concentration curve that is obtained from the biodistribution study. Values are calculated based on the trapezoidal rule up to 24 h after intravenous injection. [b] Tumor selectivity of ADR and the micelles was determined by calculating the relative accumulated concentrations between the tumor tissues and each organ (AUC_{tumor}/AUC_{organ}). Their ratios indicate the change in the tumor selectivity of the micelles with respect to ADR.

accumulate in the tumor tissues enter the cells and release the drugs intracellularly as long as they were present in the blood. A phase-contrast image showed that the tumor blood vessels containing the micelles begin to leak into the extravascular compartment of the solid tumors (note the red color of the micelles). However, no fluorescence was detected at the corresponding part but in the limited regions of the solid tumor. Therefore, even though colloidal drug carriers are generally considered to localize in the limited peripheral regions of the solid tumors due to poor accessibility, we have confirmed that the micelles can infiltrate into tumor tissues after accumulation, thus increasing the local drug concentration. This conclusion is in good accordance with the results from the permeability testing of the micelles into MCTS.

DISCUSSION

This paper has revealed a new potency of the polymeric micelle drug carrier systems that they can directly deliver drugs to the interior of targeted cells in vivo by infiltrat-

Table 4. Tissue-to-blood Concentration Ratio (K_b) in Each Organ[a]

	organ				
time (h)	tumor	heart	kidney	liver	spleen
0.5	0.0545	0.0714	0.168	0.0946	0.1023
1	0.0976	0.0772	0.1903	0.1429	0.1617
3	0.134	0.0755	0.1402	0.1834	0.2136
6	0.1747	0.0764	0.1226	0.2141	0.2651
9	0.2412	0.0762	0.134	0.3014	0.3859
24	0.5992	0.0761	0.1162	0.7037	0.9158

[a] K_b value is defined as $[K_b = C_{tissue}/C_{blood}]$ where C_{tissue} and C_{blood} were the tissue concentration and the blood concentration of the micelles, respectively. Each K_b value indicates the distribution of the drugs in vascular space ($K_b < 0.1$), extracellular space ($0.1 < K_b < 0.5$), and intracellular space ($0.5 < K_b$).

ing into solid tumors. These findings provided a clear answer to the questions whether the nanosized supramolecular drug carriers can access the cells in the avascular region of the solid tumors without structural and functional breakdown, which is also crucial to other intracellular environment-sensitive macromolecular bioconjugates that are injected through the vein for tumor targeting.

For the past several decades, natural and artificial macromolecules have evolved into a very useful class of drug delivery media (*36*–*39*). However, their in vivo applications are not always successful because limited accessibility inside solid tumors causes stagnation of drug carriers at the periphery of the tumor vasculatures, inducing low concentrations of active drugs in the targeted tumor tissues (*40*). Such a poor delivery efficiency of active drugs to the solid tumors is considered a serious problem facing recent cancer therapy using drug carriers. In this regard, we considered that the intrinsic characteristics of drug carriers may play a critical role in determining their in vivo behaviors, such as tumor permeability, drug release property, and antitumor activity. To confirm this, a suitable carrier model is required that controls the release of drugs while its structural features are optimized for a tumor-targeting drug delivery, and we prepared a new type of drug carrier in this study by adding an intracellular pH-triggered drug release property to the polymeric micelle drug carrier system whose chemical and biological properties are clearly identified (*41*).

As shown in the experimental results, the prepared micelle behaves not only as a biocompatible nanosized drug carrier with a high drug-loading content but also as a bioresponsive device with intracellular pH-sensitivity to control the drug release. These characteristic behaviors suggest that the nanosized core−shell structure of the micelles seems important to take the best advantage of the PEG shielding, imparting both stability and fragility into a single carrier system. The micelles safely protect the loaded drugs and functional linkers by providing a nanocompartment in the core that is completely segregated from the external environments; they maintain a high water-solubility with the hydrophilic shell that prevents the adsorption of proteins and the adhesion of cells so as to circumvent the uptake by reticuloendothelial systems during blood circulation (*42*, *43*). In the meantime, intracellular trafficking of the micelles in the solid tumors is evident, which indicates that PEG shielding of the micelle may behave as a kinetic barrier that regulates the condition of the molecular affinity interaction between the micelles and cell membrane according to the exposure or retention time. As explained by the EPR effect, solid tumors feature a large vascular permeability, high interstitial diffusivity, and poor lymphatic drainage; this is a fact that results in tumor-specific retention over a long period of time required for interacting with tumor cells. The retention time in each organ influences the intracellular trafficking of the micelles; thereby, any undesirable cytotoxicity to the normal organs is avoided. Consequently, the intracellular pH-triggered drug release property of the micelles should be the major reason for in vivo antitumor activity with low toxicity.

In conclusion, the intracellular pH-sensitive polymeric micelles exemplify the supramolecular drug carriers that control the systemic, local, and subcellular distribution of the active drugs. They show a higher bioavailability than free drugs, and therefore, the intracellular delivery of drugs would be the most effective and promising formulation for cancer chemotherapy with enhanced therapeutic efficacy and low toxicity. Moreover, the study reveals that the biocompatible structure and environment-sensitive functionality should be considered as a single event in order to realize the carrier systems that are related to these intracellular environments and material transports for the future treatment of cancers with avascular tumor tissue.

ACKNOWLEDGMENT

This research was supported by a Grant-in-Aid for Scientific Research from the Ministry of Education, Culture, Sports, Science and Technology (MEXT), Japan, and by Core Research for Evolutional Science and Technology (CREST), Japan Science and Technology Corporation (JST).

Supporting Information Available: Synthetic scheme for PEG-p(Asp-Hyd-ADR) block copolymer. HPLC analysis protocol for biodistribution. This material is available free of charge via the Internet at http://pubs.acs.org.

LITERATURE CITED

(1) Duncan, R. (2003) The dawning era of polymer therapeutics. *Nat. Rev. Drug Discovery 2*, 347−360.
(2) Maeda, H. (2001) SMANCS and polymer-conjugated macromolecular drugs advantages in cancer chemotherapy. *Adv. Drug Delivery Rev. 46*, 169−185.
(3) Jain, R. K. (2001) Delivery of molecular and cellular medicine to solid tumors. *Adv. Drug Delivery Rev. 46*, 149−168.
(4) Kopecek, J. (2003) Smart and genetically engineered biomaterials and drug delivery systems. *Eur. J. Pharm. Sci. 20*, 1−16.
(5) Nishiyama, N., Okazaki, S., Cabral, H., Miyamoto, M., Kato, Y., Sugiyama, Y., Nishio, K. Matsumura, Y., and Kataoka, K. (2003) Novel cisplatin-incorporated polymeric micelles can eradicate solid tumors in mice. *Cancer Res. 63*, 8977−8983.
(6) Lewanski, C. R. I., and Stewart, S. (1999) PEGylated liposomal adriamycin: a review of current and future applications. *Pharm. Sci. Technol. Today 2*, 473−477.
(7) Jensen, K. D., Nori, A., Tijerina, M., Kopeckova, P., and Kopecek, J. (2003) Cytoplasmic delivery and nuclear targeting of synthetic macromolecules. *J. Controlled Release 87*, 89−105.
(8) Lian, T., and Ho, R. J. Y. (2001) Trends and developments in liposome drug delivery systems. *J. Pharm. Sci. 90*, 667−680.
(9) Kataoka, K., Kwon, G., Yokoyama, M., Okano, T., and Sakurai, Y. (1993) Block-copolymer micelles as vehicles for drug delivery. *J. Controlled Release 24*, 119−132.
(10) Ringsdorf, H. (1975) Structure and properties of pharmacologically active polymers. *J. Polym. Sci. Polym. Symp. 51*, 135−153.

(11) Vasey, P. A., Kaye, S. B., Morrison, R., Twelves, C., Wilson, P., Duncan, R., Thomson, A. H., Murray, L. S., Hilditch, T. E., Murray, T., Burtles, S., Fraier, D., Frigerio, E., and Cassidy, J. (1999) Phase I clinical and pharmacokinetic study of PK1 [N-(2-hydroxypropyl)methacrylamide copolymer doxorubicin]: first member of a new class of chemotherapeutic agents – drug-polymer conjugates. *Clin. Cancer Res. 5*, 83–94.

(12) Gordon, A. N., Fleagle, J. T., Guthrie, D., Parkin, D. E., Gore, M. E., and Lacave, A. J. (2001) Recurrent epithelial ovarian carcinoma: a randomized phase III study of pegylated liposomal doxorubicin versus topotecan. *J. Clin. Oncol. 19*, 3312–3322.

(13) Nakanishi, T., Fukushima, S., Okamoto, K., Suzuki, M., Matsumura, Y., Yokoyama, M., Okano, T., Sakurai, Y., and Kataoka, K. (2001) Development of the polymer micelle carrier system for doxorubicin. *J. Controlled Release 74*, 295–302.

(14) Jain, R. K. (1994) Barriers to drug delivery in solid tumors. *Sci. Am. 271*, 58–65.

(15) Takakura, Y., and Hashida, M. (1996) Macromolecular carrier systems for targeted drug delivery: Pharmacokinetic considerations on biodistribution. *Pharm. Res. 13*, 820–831.

(16) Dvorak, H. F., Nagy, J. A., Dvorak, J. T., and Dvorak, A. M. (1998) Identification and characterization of the blood vessels of solid tumors that are leaky to circulating macromolecules. *Am. J. Pathol. 133*, 95–109.

(17) Ishida, T., Kirchmeier, M. J., Moase, E. H., Zalipsky, S., and Allen, T. M. (2001) Targeted delivery and triggered release of liposomal doxorubicin enhances cytotoxicity against human B lymphoma cells. *Biochim. Biophys. Acta Biomembranes 1515*, 144–158.

(18) Tsukioka, Y., Matsumura, Y., Hamaguchi, T., Koike, H., Moriyasu, F., and Kakizoe, T. (2002) Pharmaceutical and biomedical differences between micellar doxorubicin (NK911) and liposomal doxorubicin (Doxil). *Jpn. J. Cancer Res. 93*, 1145–1153.

(19) Unezaki. S., Maruyama, K., Hosoda, J., Nagae, I., Koyanagi, Y., Nakata, M., Ishida, O., Iwatsuru, M., and Tsuchiya, S. (1996) Direct measurement of the extravasation of poly(ethyleneglycol)-coated liposomes into solid tumor tissue by in vivo fluorescence microscopy. *Int. J. Pharm. 144*, 11–17.

(20) Suzuki, H., Nakai, D., Seita, T., and Sugiyama, Y. (1996) Design of a drug delivery system for targeting based on pharmacokinetic consideration. *Adv. Drug Delivery Rev. 19*, 335–357.

(21) Jones, A. T., Gumbleton, M., and Duncan, R. (2003) Understanding endocytic pathways and intracellular trafficking: a prerequisite for effective design of advanced drug delivery systems. *Adv. Drug Delivery Rev. 55*, 1353–1357.

(22) Bae, Y., Fukushima, S., Harada, A., and Kataoka, K. (2003) Design of environment-sensitive supramolecular assemblies for intracellular drug delivery: polymeric micelles that are responsive to intracellular pH change. *Angew. Chem., Int. Ed. 42*, 4640–4643.

(23) D'souza, A. J. M., and Topp, E. M. (2004) Release from polymeric prodrugs: linkages and their degradation. *J. Pharm. Sci. 93*, 1962–1979.

(24) Ulbrich, K., and Subr, V. (2004) Polymeric anticancer drugs with pH-controlled activation. *Adv. Drug Delivery Rev. 56*, 1023–1050.

(25) Willner, D., Trail, P. A., Hofstead, S. J., King, H. D., Lasch, S. J., Braslawsky, G. R., Greenfield, R. S., Kaneko, T., Firestone, R. A. (1993) (6-Maleimidocaproyl)hydrazone of doxorubicin. A new derivative for the preparation of immunoconjugates of doxorubicin. *Bioconjugate Chem. 4*, 521–527.

(26) Kaneko, T., Willner, D., Monkovic, I., Knipe, J. O., Braslawsky, G. R., Greenfield, R. S., and Vyas D. M. (1991) New hydrazone derivatives of adriamycin and their immunoconjugates – a correlation between acid stability and cytotoxicity. *Bioconjugate Chem. 2*, 133–141.

(27) Hamilton, G. (1998) Multicellular spheroids as an in vitro tumor model. *Cancer Lett. 131*, 29–34.

(28) Sutherland, R. M. (1988) Cell and environment interactions in tumor microregions: the multicell spheroid model. *Science 240*, 177–184.

(29) Konerding, M. A., Fait E., and Gaumann, A. (2001) 3D microvascular architecture of pre-cancerous lesions and invasive carcinomas of the colon. *Br. J. Cancer 84*, 1354–1362.

(30) Maeda, H., Wu, J., Sawa, T., Matsumura, Y., and Hori, K. (2000) Tumor vascular permeability and the EPR effect in macromolecular therapeutics: a review. *J. Controlled Release 65*, 271–284.

(31) Matsumura, Y., and Maeda, H. (1986) A new concept of macromolecular therapeutics in cancer chemotherapy: mechanism of tumoritropic accumulation of proteins and the antitumor agent SMANCS. *Cancer Res. 46*, 6387–6392.

(32) Jain, R. K. (1988) Determinants of tumor blood flow: a review. *Cancer Res. 48*, 2641–2658.

(33) Baxter, L. T., Daniel, H. Z., Mackensen, G., and Jain, R. K. (1994) Physiologically based pharmacokinetic model for specific and nonspecific monoclonal antibodies and fragments in normal tissues and human tumor xenografts in nude mice. *Cancer Res. 54*, 1517–1528.

(34) Yamamoto, Y., Nagasaki, Y., Kato, Y., Sugiyama, Y., and Kataoka, K. (2001) Long-circulating poly(ethylene glycol)-poly(D, L-lactide) block copolymer micelles with modulated surface charge. *J. Control. Release 77*, 27–38.

(35) Nishiyama, N., Kato, Y., Sugiyama, Y., and Kataoka, K. (2001) Cisplatin-loaded polymer–metal complex micelle with time-modulated decaying property as a novel drug delivery system. *Pharmaceut. Res. 18*, 1035–1041.

(36) Torchilin, V. P., Lukyanov, A. N., Gao, Z. G., and Papahadjopoulos-Sternberg, B. (2003) Immunomicelles: Targeted pharmaceutical carriers for poorly soluble drugs. *P. Natl. Acad. Sci. USA. 100*, 6039–6044.

(37) Adams, M. L., Lavasanifar, A., and Kwon, G. (2003) Amphiphilic block copolymers for drug delivery. *J. Pharm. Sci. 92*, 1343–1355.

(38) Shiah, J. G., Dvorak, M., Kopeckova, P., Sun, Y., Peterson, C. M., and Kopecek, J. (2001) Biodistribution and antitumour efficacy of long-circulating N-(2-hydroxypropyl)methacrylamide copolymer-doxorubicin conjugates in nude mice. *Eur. J. Cancer 37*, 131–139.

(39) Kopecek, J., Kopeckova, P., Minko, T., Lu, Z. R., and Peterson, C. M. (2001) Water soluble polymers in tumor targeted delivery. *J. Controlled Release 74*, 147–158.

(40) Emanuel, N., Kedar, E., Bolotin, E. M., Smorodinsky, N. I., and Barenholz, Y. (1996) Targeted delivery of doxorubicin via sterically stabilized immunoliposomes: Pharmacokinetics and biodistribution in tumor-bearing mice. *Pharm. Res. 13*, 861–868.

(41) Kataoka, K., Harada, A., and Nagasaki, Y. (2001) Block copolymer micelles for drug delivery: design, characterization and biological significance. *Adv. Drug. Delivery Rev. 47*, 113–131.

(42) Yokoyama, M., Okano, T., Sakurai, Y., Fukushima, S., Okamoto, K., and Kataoka, K. (1999) Selective delivery of adriamycin to a solid tumor using a polymeric micelle carrier system. *J. Drug Target. 7*, 171–186.

(43) Kwon, G., Suwa, S., Yokoyama, M., Okano, T., Sakurai, Y., and Kataoka, K. (1994) Enhanced tumor accumulation and prolonged circulation times of micelle-forming poly(ethylene oxide-aspartate) block copolymer-adriamycin conjugates. *J. Controlled Release 29*, 17–23.

BC0498166

Drug Delivery

Supramolecular Nanocarrier of Anionic Dendrimer Porphyrins with Cationic Block Copolymers Modified with Polyethylene Glycol to Enhance Intracellular Photodynamic Efficacy**

*Woo-Dong Jang, Nobuhiro Nishiyama, Guo-Dong Zhang, Atsushi Harada, Dong-Lin Jiang, Satoko Kawauchi, Yuji Morimoto, Makoto Kikuchi, Hiroyuki Koyama, Takuzo Aida, and Kazunori Kataoka**

A great number of challenges have been overcome to create efficient photosensitizers (PSs) for photodynamic therapy (PDT) which have a high photocytotoxicity and selectivity for

[*] Dr. W.-D. Jang, Dr. N. Nishiyama, Dr. G.-D. Zhang, Dr. A. Harada, Prof. Dr. K. Kataoka
Department of Materials Science and Engineering
Graduate School of Engineering, The University of Tokyo
7-3-1 Hongo, Bunkyo-ku, Tokyo 113-8656 (Japan)
Fax: (+81) 3-5841-7139
E-mail: kataoka@bmw.t.u-tokyo.ac.jp
Dr. D.-L. Jiang, Prof. Dr. T. Aida
Department of Chemistry and Biotechnology
Graduate School of Engineering, The University of Tokyo
7-3-1 Hongo, Bunkyo-ku, Tokyo 113-8656 (Japan)
Dr. W.-D. Jang, Dr. G.-D. Zhang, Dr. A. Harada, Prof. Dr. K. Kataoka
CREST
Japan Science and Technology Corporation (Japan)
Dr. N. Nishiyama, Dr. H. Koyama
Department of Clinical Vascular Regeneration
Graduate School of Medicine, The University of Tokyo
7-3-1 Hongo, Bunkyo-ku, Tokyo 113-8655 (Japan)
Dr. S. Kawauchi, Dr. Y. Morimoto, Prof. Dr. M. Kikuchi
Department of Medical Engineering
National Defense Medical College
3-2 Namiki, Tokorozawa, Saitama, 359-8513 (Japan)

[**] This work was supported by Core Research for Evolutional Science and Technology (CREST), JST.

 DOI: 10.1002/anie.200461603 © 2005 Wiley-VCH Verlag GmbH & Co. KGaA, Weinheim

the diseased tissue.[1] To obtain high quantum yields and effective energy absorption, PSs generally need to have large π-conjugation domains such as a porphyrin structure. Therefore, most conventional PSs easily form aggregates, which produce a self-quenching effect of the excited state, in aqueous medium as a result of their π–π interactions and hydrophobic characteristics. These issues can be overcome, as we reported previously, by segregating PSs into the focal core of dendrimers (dendrimer porphyrins (DPs), Figure 1b).[2] DPs are attractive for biomedical purposes because of their predictable structures, that is, their monodisperse molecular weight and tunable three-dimensional structures, and their flexibility for a high density of tailored functional groups on the periphery.[3] Indeed, third-generation DPs with 32 cationic or anionic peripheral groups exhibit a high solubility in aqueous medium and have a high quantum yield for the generation of singlet oxygen, which leads to an appreciable photocytotoxicity.[2] These advantageous features of DPs are facilitated to an even greater extent by their inclusion into stealth nanocarriers, thus improving their longevity in blood circulation and results in their gradual accumulation in solid tumors through the enhanced permeation and retention (EPR) effect.[4] Furthermore, as demonstrated here, the inclusion of DPs into a novel type of nanocarrier, that is, polymeric micelles, has led to an unprecedented increase in the photocytotoxicity without compromising either the photophysical properties of DPs in regard to their efficient photochemical reactions or the physicochemical properties of the carriers necessary for tumor-selective delivery.

A novel polymeric micelle system[5] for PDT is based on an electrostatic assembly of an anionic DP,[6] which consists of zinc porphyrin at the focal core with a third generation of poly(benzyl ether) dendritic frameworks having 32 negative charges on the periphery, and poly(ethylene glycol)–poly(L-lysine) block copolymer (PEG-*b*-PLL) in aqueous media (polyion complex (PIC) micelles; Figure 1b).[7] The DP-incorporated micelles (DP/m), prepared with a stoichiometric ratio of negatively charged DP and positively charged PEG-*b*-PLL, were approximately 64 nm in diameter with an extremely narrow size distribution in physiological saline solution (Figure 2a). Our previous study using static light scattering (SLS) measurements demonstrated that an individual DP/m contains an average of 38 DP molecules and the micelles have a remarkable stability against salt concentrations,[7] which indicates the clear stabilization effect by the 32 negative charges of DP in the micellar structure. The dependency of the formation of DP/m on the pH value was investigated by dynamic and static light scattering (DLS and SLS) measurements. Figure 2b shows the pH-dependent changes in the translational diffusion coefficient (D_T) and normalized $(Kc/\Delta R(0))^{-1}$ (normalized to the micelle at pH 7.4) of DP/m, where D_T is related to the hydrodynamic size based on the Stokes–Einstein equation, and the normalized $(Kc/\Delta R(0))^{-1}$ value is related to the changes in the average apparent molecular weight of the micelles. Both the hydrodynamic size and normalized $(Kc/\Delta R(0))^{-1}$ value basically remained unchanged in the pH range from 6.4 to 8.5 (Figure 2b). However, the diameter of the micelles gradually

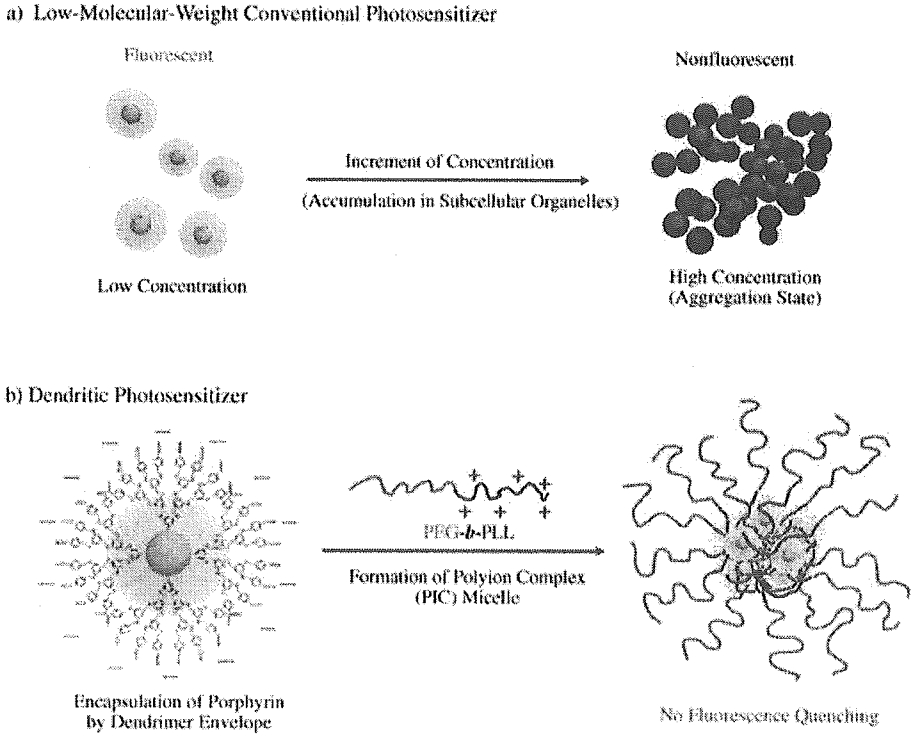

Figure 1. a) Conventional PS aggregate at a high concentration which results in quenching of PSs. b) Formation of polyion complex (PIC) micelles through electrostatic assembly of anionic dendrimer porphyrins (DPs) and PEG-*b*-PLL copolymers. The dendrimer envelope of DP can sterically prevent aggregation of the center porphyrin, thus there is no fluorescence quenching of the center porphyrin.

 © 2005 Wiley-VCH Verlag GmbH & Co. KGaA, Weinheim

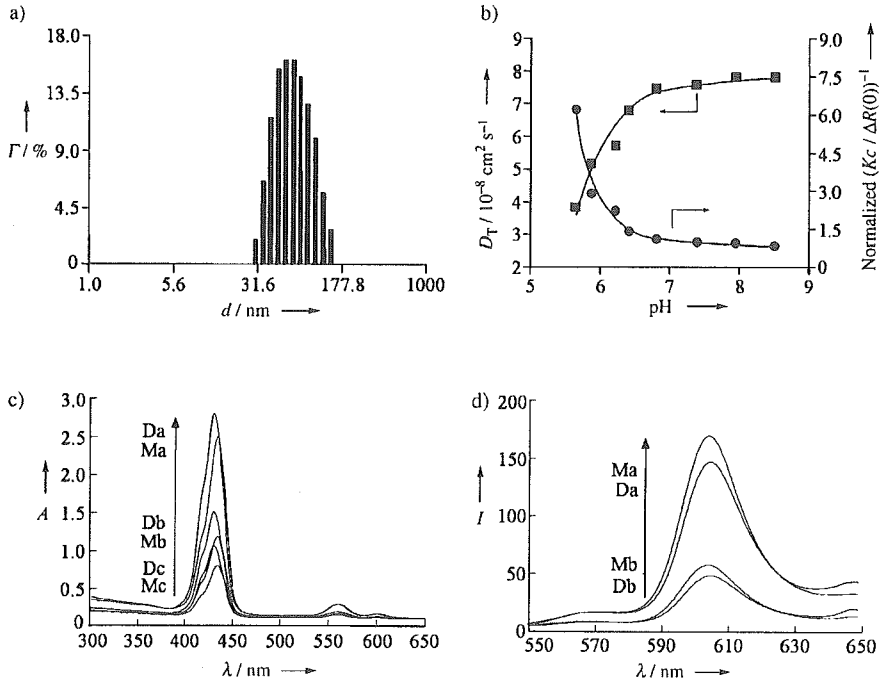

Figure 2. Physical properties of DP and DP/m. a) DLS histogram of DP/m in 150 mM NaCl at 25 °C; d = diameter. b) Dependency of the translational diffusion coefficients D_T (■) and normalized $(Kc/\Delta R(0))^{-1}$ (●) on the pH value for DP/m (1 mg mL^{-1}), measured by DLS and SLS, respectively, at 25 °C. c) Electronic absorption spectra of DP alone and DP/m in PBS (pH 7.4; a = 12 μM, b = 4 μM, c = 2 μM, D: DP, M: DP/m). d) Fluorescence emission spectra of DP alone and DP/m in PBS (pH 7.4; a = 12 μM, b = 4 μM, D: DP, M: DP/m).

increased with an increased apparent molecular weight below pH 6.4 (Figure 2b), and finally precipitated at pH 5.6, which indicates the acid-responsive feature of the micelles. Protonation of DP occurred under acidic pH conditions and resulted in the diminution of the electrostatic interaction between DP and PEG-*b*-PLL. Thus, the well-defined core–shell structure may become more diffuse and a merging of the micelles may take place. This pH-responsive behavior of the micelles allows their effective accumulation in solid tumors in response to the low pH value of the tumor tissue[8] or in an endosomal compartment in the tumor cells while achieving stable circulation in the bloodstream.

The electronic absorption and emission spectra of DP and DP/m are shown in Figure 2c and d, respectively. Unlike low-molecular-weight PSs,[9] DP clearly maintained its absorption and emission intensity in spite of the formation of micelles. The incorporation of DP into the micelles resulted in a 5-nm red-shift for the Soret band of the porphyrin core and a hypochromicity of about 5% (Figure 2c). Both of these effects are likely to be caused by the formation of an electrostatic assembly of charged porphyrins and oppositely charged compounds.[10] The shrinkage of the hydrophobic dendrimer frameworks, which arises from the relaxation of the charge repulsion of the negatively charged DP surface by the formation of an electrostatic assembly, may contribute to the hypochromicity.[11] Interestingly, although the local concentration of DP within each micelle is assumed to be extremely high, DP/m emitted a more intense fluorescence at 610 nm (Figure 2d). Unlike conventional PSs, the dendritic envelope of DP is able to prevent the porphyrin core from undergoing collisional quenching, even at an appreciably high concentration that induces self-quenching of the conventional PSs (Figure 1a).[12] Thus, encapsulation of the porphyrins by the dendritic envelope in the micellar structure is most likely to prevent fluorescence quenching (Figures 1b and 2d). Also, the high microviscosity in the micellar core could restrain the internal molecular motion of DP, which might lead to the inhibition of the nonradiative decay and is related to the increased fluorescence intensity of DP/m (Figure 2d).[13] In connection with this observation, the photoinduced oxygen consumption of DP and DP/m was measured in phosphate-buffered saline (PBS) containing 10% fetal bovine serum (FBS) as a singlet oxygen acceptor (Figure 3). Very interestingly, the result revealed that the oxygen consumption level of

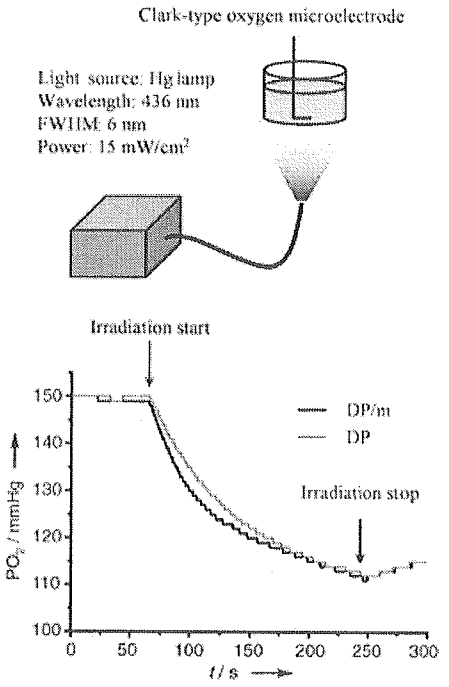

Figure 3. Experimental setup for the measurement of oxygen consumption and the results obtained. FWHM = full width of half maximum height.

© 2005 Wiley-VCH Verlag GmbH & Co. KGaA, Weinheim

DP/m was almost identical to that of the free DP in PBS, which indicates that the singlet oxygen molecules can successfully escape the micellar structure. From the standpoint of the application to PDT, the DP ensures an effective photochemical reaction of the porphyrin core regardless of the local concentrations. It is possible that the DP/m attain an elevated concentration of local singlet oxygen, which cannot be achieved by other formulations containing conventional PSs.

However, the cellular uptake of free DP and DP/m increased with the incubation time, and DP/m showed six- to eightfold higher uptake levels than free DP (Figure 4a). In

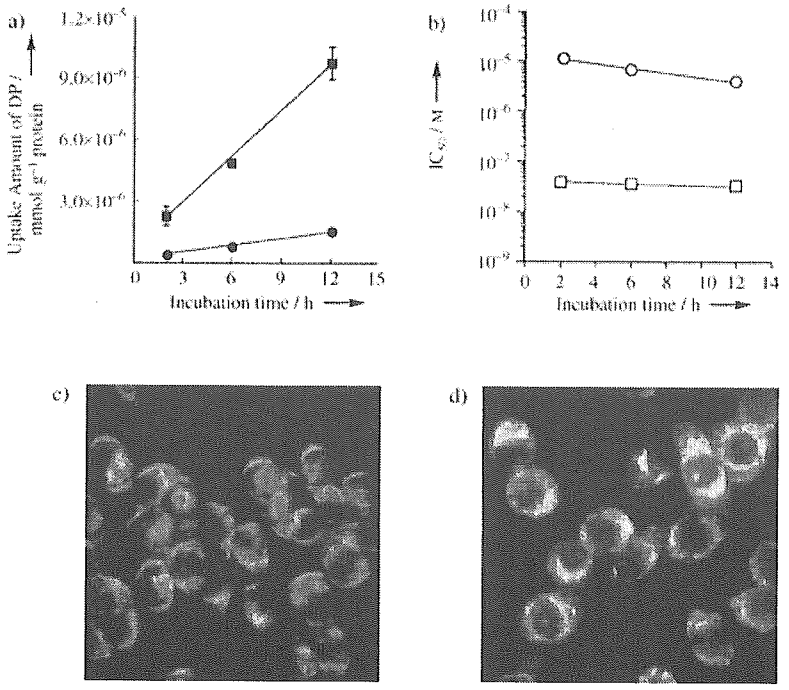

Figure 4. Results of in vitro evaluations of DP and DP/m. a) Cellular uptake level of DP (●) and DP/m (■) as a function of incubation time ($n = 3$). LLC cells were incubated with dendrimers and the micelles at 12 μM of DP-equivalent concentration. b) Incubation time dependency of 50% growth inhibitory concentration (IC_{50}) of DP (○) and DP/m (□) after photoirradiation. c,d) Microscopy images of LLC cells incubated with 10 μM of DP (c) and DP/m (d) for 8 h. A Zeiss filter set (excitation: BP 395–440 nm; beam splitter: FT 460 nm; emission: LP 470 nm) was used.

view of the negatively charged surface of mammalian cells,[8] charge neutralization of DP by PEG-*b*-PLL could improve the cellular uptake of DP/m. The improved uptake of DP/m was also confirmed by microscopic observations (Figure 4c and d). No fluorescence quenching was observed for the cells incubated with DP/m, although the sensitizers are assumed to be extremely concentrated in the subcellular organelles such as the endosomes and lysosomes. This observation contrasts with the fact that the conventional mesochlorin e_6 conjugated *N*-(2-hydroxypropyl) methacrylamide (HPMA) copolymers exhibit fluorescence quenching when the cells are incubated with HPMA at an extremely high concentration.[14] The dendritic envelope of DP could prevent aggregation of the porphyrin in the subcellular loci, thus ensuring effective production of singlet oxygen for the photocytotoxicity.

Notably, the photocytotoxicity of DP/m was remarkably improved compared to that of free DP (Figure 4b). Incorporation of DP into the micelles resulted in an approximately 130–280-fold increased photocytotoxicity (Figure 4b). Such a distinctly enhanced photocytotoxicity of DP/m may not be fully explained by the six- to eightfold increase in their cellular uptake shown in Figure 4a; therefore, DP/m may have specific mechanisms to increase their photocytotoxicity. Recently, PEGylated chlorin e_6 and PEG-based polymeric micelles were reported to show an enhanced localization in several cytoplasmic organelles including the mitochondria.[15] Presumably the outer PEG layer of the DP/m and the microenvironment around DP, as mentioned above, may have a role in altering the intracellular mechanism of DP to increase the photocytotoxicity. Recently, several interesting observations concerning the intracellular mechanism have been reported. For example, Berg et al. proposed a photochemical internalization (PCI) in which the photodamage to endosomal membranes can burst the endocytic vesicles, which allows endosomal escape of macromolecules into the cytosol.[16] From this point of view, DP/m may localize in the cytoplasmic organelles susceptible to photodamage following endosomal escape of the micelles during photoirradiation. The DP/m are assumed to produce a significantly high concentration of singlet oxygen as a result of effective separation of the center porphyrin by the dendritic envelope. The mechanism for the efficient generation of singlet oxygen within the micellar structure remains to be explained. However, a dendritic structure that prevents aggregation of the center porphyrin should be essential for the enhanced photocytotoxicity of DP/m. Further investigation to address the detailed mechanisms of the enhanced photocytotoxicity of DP/m, together with dendrimer size and morphological effect, is now in progress.

In summary, the photodynamic efficacy of the DP was dramatically improved by inclusion into micelles. This process resulted in a more than two orders of magnitude increase in the photocytotoxicity compared with that of the free DP, as a result of the accumulated singlet oxygen in the intracellular compartment as well as the modulated intracellular localization related to the micellar structure. Furthermore, the DP/m system has a relevant size range (ca. 100 nm) and high stability for intravenous administration, with resultant EPR effect, and may have a high utility for in vivo PDT of cancer and macular degeneration, the study of which is now in progress.

Experimental Section

PEG-*b*-PLL was synthesized by the polymerization of the *N*-carboxy anhydride of N^{ε}-Z-L-lysine initiated by CH_3O-PEG-NH_2 (12000 g mol^{-1}) in DMF, followed by deprotection of the Z group according to a previously reported method.[17] The M_w/M_n ratio and degree of polymerization of PLL were determined to be 1.11:1 and 41 by gel-permeation chromatography and ^{1}H NMR spectroscopy,

 © 2005 Wiley-VCH Verlag GmbH & Co. KGaA, Weinheim

respectively. DP was synthesized as previously described,[6] and its purity was confirmed by a single peak in the MALDI-TOF mass spectrum (8030 $g\,mol^{-1}$). The DLS and SLS measurements of DP/m were performed using a Photal dynamic laser-scattering DLS-7000 spectrometer (Otsuka Electronics Co., Ltd., Osaka, Japan). The UV/Vis and fluorescence spectra were measured on a V-550 spectrophotometer and on an FP-777 spectrofluorometer (JASCO, Tokyo, Japan), respectively.

Lewis lung carcinoma (LLC) cells were used in the cell culture studies. In the quantitative analysis of the cellular uptake of DP, the cells incubated with free DP and DP/m were lyzed in 5% SDS solution, followed by measurement of the fluorescence intensity at 609 nm (excitation at 432 nm). In the cytotoxicity assay, the cells were photoirradiated for 10 minutes with broadband visible light using a xenon lamp (150 W) equipped with a filter passing light of 400–700 nm (fluence energy: 180 $kJ\,cm^{-2}$). The viability of the cells was evaluated by the 3-(4,5-dimethylthiazol-2-yl)-2,5-diphenyltetrazolium bromide (MTT) assay.

Oxygen consumption was measured by using a Clark-type oxygen microelectrode with a tip diameter of 200 μm (PO_2-100DW, Eikou Kagaku Co., Ltd., Tokyo, Japan). The microelectrode was inserted into the PBS, which contained 3.13 μM of DP or DP/m and 10% FBS as a singlet oxygen acceptor, so that the tip was 100 mm above the bottom of the solution. An Hg lamp (436 nm, FWHM: 6 nm, 15 $mW\,cm^{-2}$) was used for light irradiation. The solution was static and exposed to the atmosphere. Before each measurement, the system was calibrated in saline solution bubbled with air, in which the oxygen partial pressure was assumed to be 150 mm Hg.

Received: August 10, 2004

Keywords: block copolymers · dendrimers · drug delivery · micelles · porphyrinoids

[1] R. K. Pandey, G. Zhang in *Porphyrin Handbook, Vol. 6* (Eds.: K. M. Kadish, K. M. Smith, R. Guilard), Academic Press, **2000**, pp. 157–230.
[2] N. Nishiyama, H. R. Stapert, G. D. Zhang, D. Takasu, D. L. Jiang, T. Nagano, T. Aida, K. Kataoka, *Bioconjugate Chem.* **2003**, *14*, 58–66.
[3] a) A. W. Bosman, H. M. Jassen, E. W. Meijer, *Chem. Rev.* **1999**, *99*, 1665–1688; b) S. Hecht, J. M. J. Frechet, *Angew. Chem.* **2001**, *113*, 76–94; *Angew. Chem. Int. Ed.* **2001**, *40*, 74–91; c) M. Fischer, F. Vogtle, *Angew. Chem.* **1999**, *111*, 934–955; *Angew. Chem. Int. Ed.* **1999**, *38*, 884–905; d) H. R. Ihre, L. Gagne, J. M. J. Frechet, F. C. Szoka, Jr., *Bioconjugate Chem.* **2002**, *13*, 453–461; e) J. F. Kukowska-Latallo, A. U. Bielinska, J. Johnson, R. Spindler, D. A. Tomalia, J. R. Baker, *Proc. Natl. Acad. Sci. USA* **1996**, *93*, 4897–4902.
[4] a) Y. N. Konan, R. Gurny, E. Allemann, *J. Photochem. Photobiol. B* **2002**, *66*, 89–106; b) Y. Matsumura, H. Maeda, *Cancer Res.* **1986**, *46*, 6387–6392; c) M. Yokoyama, T. Okano, Y. Sakurai, S. Fukushima, K. Okamoto, K. Kataoka, *J. Drug Targeting* **1999**, *7*, 171–186.
[5] Y. Kakizawa, K. Kataoka, *Adv. Drug Delivery Rev.* **2002**, *54*, 203–222, and references therein.
[6] a) N. Tomioka, D. Takasu, T. Takahashi, T. Aida, *Angew. Chem.* **1998**, *110*, 1611–1614; *Angew. Chem. Int. Ed.* **1998**, *37*, 1531–1534; b) T. Aida, D.-L. Jiang in *The Porphyrin Handbook, Vol. 3* (Eds: K. M. Kadish, K. M. Smith, R. Guilard), Academic Press, **2003**, pp. 369–384.
[7] H. R. Stapert, N. Nishiyama, D. L. Jiang, T. Aida, K. Kataoka, *Langmuir* **2000**, *16*, 8182–8188.
[8] a) E. J. Ambros, D. M. Easty, P. C. T. Jones, *Br. J. Cancer* **1958**, *12*, 439–447; b) S. E. Kornguth, T. Kalinke, H. I. Robins, J. D. Cohen, P. Turski, *Cancer Res.* **1989**, *49*, 6390–6395.
[9] S. A. Gerhardt, J. W. Lewis, D. S. Kliger, J. Z. Zhang, U. Simonis, *J. Phys. Chem. A* **2003**, *107*, 2763–2767.
[10] a) N. C. Maiti, S. Mazumdar, N. Periasamy, *J. Phys. Chem. B* **1998**, *102*, 1528–1538; b) K. M. Kadish, G. B. Maiya, C. Araullo, R. Guilard, *Inorg. Chem.* **1989**, *28*, 2725–2731.
[11] R. Sadamoto, N. Tomioka, T. Aida, *J. Am. Chem. Soc.* **1996**, *118*, 3978–3979.
[12] T. Sato, D.-L. Jiang, T. Aida, *J. Am. Chem. Soc.* **1999**, *121*, 10658–10659.
[13] S. Basu, *J. Photochem. Photobiol. A: Chem.* **1991**, *56*, 339–347.
[14] N. Nishiyama, A. Nori, A. Malugin, Y. Kasuya, P. Kopeckova, J. Kopecek, *Cancer Res.* **2003**, *63*, 7876–7882.
[15] a) M. R. Hamblin, J. L. Miller, T. Hasan, *Cancer Res.* **2001**, *61*, 7155–7162; b) R. Savic, L. Luo, A. Eisenberg, D. Maysinger, *Science* **2003**, *300*, 615–618.
[16] a) K. Berg, P. K. Selbo, L. Prasmickaite, T. E. Tjelle, K. Sandvig, J. Moan, G. Gaudernack, O. Fodstad, S. Kjolsrud, H. Anholt, G. H. Rodal, S. K. Rodal, A. Hogest, *Cancer Res.* **1999**, *59*, 1180–1183; b) L. Prasmickaite, A. Høgset, P. K. Selbo, B. Ø. Engesæter, M. Hellum, K. Berg, *Br. J. Cancer* **2002**, *86*, 652–657.
[17] A. Harada, K. Kataoka, *Macromolecules* **1995**, *28*, 5294–5299.

 © 2005 Wiley-VCH Verlag GmbH & Co. KGaA, Weinheim

Available online at www.sciencedirect.com

SCIENCE DIRECT®

Journal of Controlled Release 101 (2005) 223–232

journal of controlled release

www.elsevier.com/locate/jconrel

Preparation and biological properties of dichloro(1,2-diaminocyclohexane)platinum(II) (DACHPt)-loaded polymeric micelles

Horacio Cabral[a], Nobuhiro Nishiyama[b], Soichiro Okazaki[a], Hiroyuki Koyama[b], Kazunori Kataoka[a,*]

[a]*Department of Materials Science and Engineering, Graduate School of Engineering, The University of Tokyo, 7-3-1 Hongo, Bunkyo-ku, Tokyo 113-8656, Japan*

[b]*Department of Vascular Regeneration, Graduate School of Medicine, The University of Tokyo, 7-3-1 Hongo, Bunkyo-ku, Tokyo 113-8655, Japan*

Received 27 June 2004; accepted 26 August 2004
Available online 7 October 2004

Abstract

Block copolymer micelles, containing dichloro(1,2-diaminocyclohexane)platinum(II) (DACHPt), the oxaliplatin parent complex, were prepared through polymer–metal complex formation of DACHPt with poly(ethylene glycol)–poly(glutamic acid) block copolymer [PEG–P(Glu)] in distilled water. By dynamic light scattering (DLS) measurement, the micelle size was determined to be 40 nm with narrow distribution. The release of platinum complexes from the micelle core was measured in phosphate buffer saline (pH 7.4) at 37 °C. DACHPt-loaded micelle showed a sustained release rate of platinum after an induction period of 12 h. In the same conditions, the kinetic stability of DACHPt-loaded micelle was measured. The micelle was found to be very stable, keeping the initial size, for 240 h. Against murine colon adenocarcinoma 26 (C-26) cells, DACHPt-loaded micelle exhibited considerable in vitro cytotoxicity, lower than oxaliplatin but increasing with exposure time as a result of the release of platinum complexes from the micelle. In vivo biodistribution assay performed on tumor-bearing mice demonstrated that the micelle showed prolonged blood circulation due to its high stability and high tumor accumulation for a prolonged time.
© 2004 Elsevier B.V. All rights reserved.

Keywords: Polymeric micelle; Drug delivery system; Dichloro(1,2-diaminocyclohexane)platinum(II); Cancer chemotherapy; Controlled release

Abbreviations: C-26, colon adenocarcinoma 26; CDDP, *cis*-dichlorodiammineplatinum(II); DACH, diaminocyclohexane; DACHPt, dichloro(1,2-diaminocyclohexane)platinum(II); DMF, *N*,*N*-Dimethylformamide; EPR, enhanced permeability and retention; FDA, Food and Drug Administration; IC_{50}, 50% inhibitory concentration; ICP-MS, ion coupled plasma-mass spectrometry; MTT, 3-(4,5-dimethylthiazol-2-yl)-2,5-diphenyltetrazolium bromide; MWCO, molecular weight cutoff; PBLG, poly(γ-benzyl L-glutamate); PEG, poly(ethylene glycol); P(Asp), poly(aspartic acid); P(Glu), poly(glutamic acid); RES, reticuloendothelial system.

* Corresponding author. Tel.: +81 3 5841 7138; fax: +81 3 5841 7139.
E-mail address: kataoka@bmw.t.u-tokyo.ac.jp (K. Kataoka).

0168-3659/$ - see front matter © 2004 Elsevier B.V. All rights reserved.
doi:10.1016/j.jconrel.2004.08.022